Cell Reports
Medicine

Article

Discovery of galectin-8 as an LILRB4 ligand driving M-MDSCs defines a class of antibodies to fight solid tumors

Graphical abstract

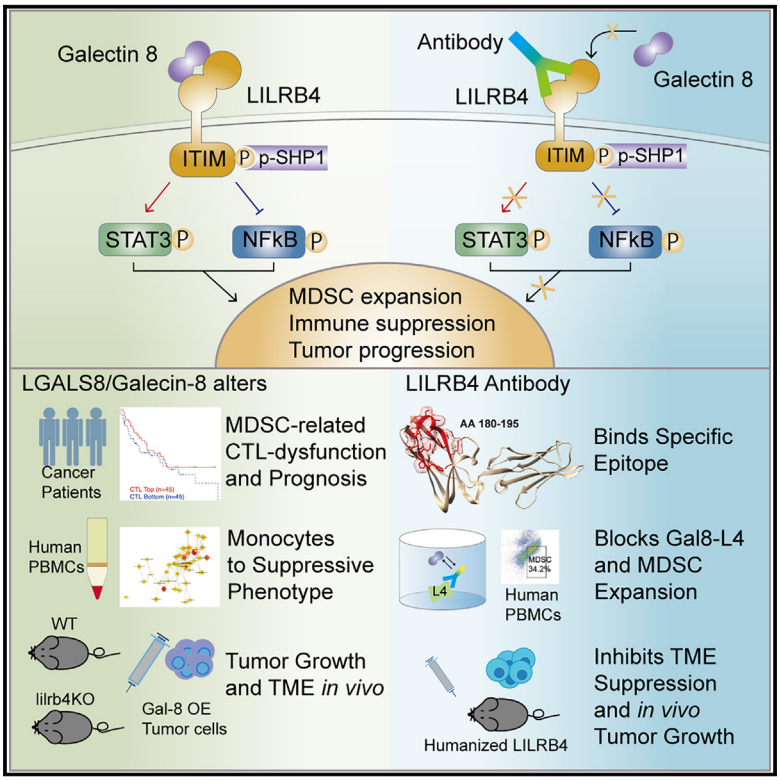

Highlights

- Galectin-8 is a functional ligand of LILRB4 that drives M-MDSCs in solid tumors
- Galectin-8-LILRB4 interaction activates STAT3 and inhibits NF-κB
- Galectin-8-LILRB4 interaction alters tumor microenvironment and promotes tumor growth
- Antibodies blocking galectin-8 and LILRB4 restrain tumor growth

Authors

Yiting Wang, Yufan Sun, Shouyan Deng, ..., Yingfei Quan, Hai Li, Jie Xu

Correspondence

jie_xu@fudan.edu.cn

In brief

Wang et al. identified galectin-8 as a functional ligand for LILRB4 that drives M-MDSCs in solid tumors, regulates the immune microenvironment, and promotes tumor growth. They further discovered downstream pathway alterations induced by this new ligand and developed blocking antibodies with well-defined epitopes and therapeutic efficacy.

Wang et al., 2024, Cell Reports Medicine 5, 101374
January 16, 2024
https://doi.org/10.1016/j.xcrm.2023.101374

CellPress

Cell Reports Medicine

CellPress
OPEN ACCESS

Article

Discovery of galectin-8 as an LILRB4 ligand driving M-MDSCs defines a class of antibodies to fight solid tumors

Yiting Wang,[1] Yufan Sun,[2] Shouyan Deng,[1] Jiayang Liu,[1] Jianghong Yu,[1] Hao Chi,[1] Xue Han,[1] Yuan Zhang,[1] Jiawei Shi,[1] Yungang Wang,[1] Yingfei Quan,[2] Hai Li,[3] and Jie Xu[1,4,*]

[1]Shanghai Xuhui Central Hospital, Zhongshan-Xuhui Hospital, and the Shanghai Key Laboratory of Medical Epigenetics, International Co-Laboratory of Medical Epigenetics and Metabolism (Ministry of Science and Technology), Institutes of Biomedical Sciences, Fudan University, Shanghai 200032, China

[2]BioTroy Therapeutics, Shanghai, China

[3]Division of Gastroenterology and Hepatology, Renji Hospital, School of Medicine, Shanghai Jiao Tong University, Shanghai, China

[4]Lead contact

*Correspondence: jie_xu@fudan.edu.cn

https://doi.org/10.1016/j.xcrm.2023.101374

SUMMARY

LILRB4 is an immunosuppressive receptor, and its targeting drugs are undergoing multiple preclinical and clinical trials. Currently, the absence of a functional LILRB4 ligand in solid tumors not only limits the strategy of early antibody screening but also leads to the lack of companion diagnostic (CDx) criteria, which is critical to the objective response rate in early-stage clinical trials. Here, we show that galectin-8 (Gal-8) is a high-affinity functional ligand of LILRB4, and its ligation induces M-MDSC by activating STAT3 and inhibiting NF-κB. Significantly, Gal-8, but not APOE, can induce MDSC, and both ligands bind LILRB4 noncompetitively. Gal-8 expression promotes *in vivo* tumor growth in mice, and the knockout of LILRB4 attenuates tumor growth in this context. Antibodies capable of functionally blocking Gal-8 are able to suppress tumor growth *in vivo*. These results identify Gal-8 as an MDSC-driving ligand of LILRB4, and they redefine a class of antibodies for solid tumors.

INTRODUCTION

T cell checkpoint immune therapies have succeeded wildly in the past decades, although only approximately 30% of patients with specific cancer types show a significant and durable response to treatment.[1,2] Mechanistic investigations have identified a group of immunosuppressive myeloid-derived cells that can limit the potency of T cell immune checkpoint blockade (ICB) therapies,[3] suggesting a compelling approach to deal with the inefficiency of T cell ICBs.[4,5] Myeloid-derived suppressive cell (MDSC), which comprises monocytic MDSC (M-MDSC) and granulocytic MDSC (G-MDSC), represents a heterogeneous population, making it difficult to identify an appropriate target.

Galectins are a family of evolutionarily conserved proteins that bind glycans and have potential roles in cancer cell survival, angiogenesis, metastasis, and immune modulation.[6–10] Although the function of galectins in immune regulation remains controversial,[10] their roles in cancer have received increasing attention.[6] Galectin-9 (Gal-9), a ligand of T cell immunoglobulin and mucin-domain containing-3 (TIM-3), was found to induce the expansion of M-MDSCs and resistance to programmed cell death protein 1 (PD-1) blockade in patients with lung cancer.[11–13] Gal-9 and Gal-8 have been identified as prognostic factors in cervical cancer and other cancer types.[14–16] Gal-8 was found to be upregulated in prostate cancer[17] and to promote cancer cell migration by binding CD166.[18] The immunomodulatory role of Gal-8 in tumors is still under debate.[16]

Leukocyte immunoglobulin-like receptor B4 (LILRB4) belongs to the leukocyte immunoglobulin (Ig)-like receptor (LILR) superfamily, which comprises type I transmembrane glycoproteins with extracellular Ig-like domains and two intracellular immunoreceptor tyrosine-based inhibitory motifs (ITIMs). LILRB4 was long regarded as an orphan receptor until apolipoprotein E (APOE) was identified as binding to LILRB4 on the surface of acute myeloid leukemia (AML) cells, promoting cancer progression and inhibiting T cells.[19] In addition to AML, LILRB4 is related to poor prognosis in solid tumors.[20] Researchers including Jim Allison and colleagues, discovered that LILRB4 acts as an immune checkpoint on MDSCs to exert immunosuppressive effects in solid tumors.[21–23] Accordingly, biopharmas, including Merck, NGM Bio, Jounce Therapeutics, and Biond Biologics, began advancing preclinical and clinical trials of anti-LILRB4 antibodies treating solid tumors.[24,25] However, the efficacy of these drugs has yet to be verified. An anti-LILRB4 antibody from NGM Bio is progressing to clinical Phase Ia, with results presented at the European Society for Medical Oncology annual meeting in November 2022.[26] According to the company's disclosure, the best overall responses were partial response in 1, stable disease

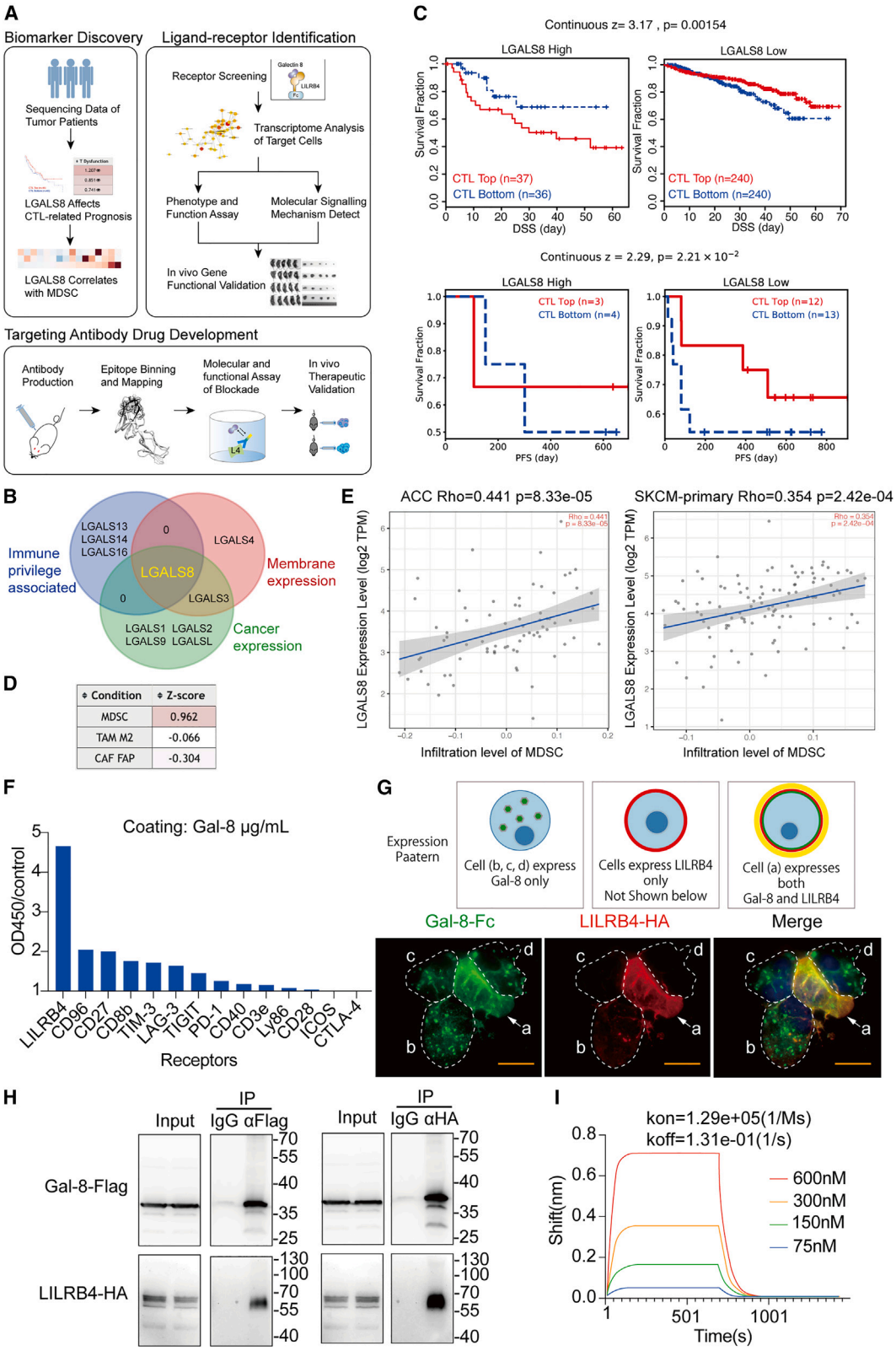

(legend on next page)

in 6, and noncomplete response/nonprogressive disease in 1 of 24 response-evaluable patients. Functional ligands for targeted receptors are often considered biomarkers for patient selection—for example, programmed death-ligand 1 (PD-L1) expression is an essential companion diagnostic (CDx) factor in clinical trials of PD-1 antibodies. Based on the results of several previous clinical trials, the objective response rate in early-stage trials is related to adequate CDx, but for LILRB4 antibodies, such a measure is missing. It is still unclear which ligand of LILRB4 may be involved in shaping the microenvironment of solid tumors, which is irrelevant to the functions of previously reported ligands or binding proteins, such as APOE, CD166, and β-amyloid.[21] Typically, one receptor binds different ligands, each inducing distinct functional effects.[27,28] Thus, the field has actively pursued a functionally relevant ligand of LILRB4 that is involved in maintaining an immunotolerant microenvironment.

In the present study, we report Gal-8 as a high-affinity, agonistic ligand of LILRB4 and characterize its role in expanding M-MDSCs and maintaining a tolerant tumor microenvironment.

RESULTS

Gal-8 associated with myeloid cell–mediated suppression in tumor microenvironment

The framework of this study is summarized in Figure 1A. A growing number of studies suggest that the galectin family plays an important role in immune escape and their role in tumor immunomodulation may be related to the selective expression of some members in immune-exempt organs such as the placenta.[29] We analyzed the expression patterns of the galectins by searching all galectin-related proteins on The Human Protein Atlas[30] (Table S1). Although there were four galectins highly expressed in immune-privileged tissues, including syncytiotrophoblasts and spermatids, only Gal-8 was highly expressed in both. Moreover, the expression of Gal-8 was highest in spermatids (Figure S1A). We additionally used the subcellular localization of the galectins and their expression in tumors to identify a specific member of the family, Gal-8 (Figure 1B; Table 1). Further studies confirmed the potential value of Gal-8 in tumor immunomodulation. Gal-8 was revealed to associate with T cell dysfunction in the tumor microenvironment, as characterized by the tumor immune dysfunction and exclusion (TIDE) model.[31] As shown in Figure 1C, in tumors expressing low levels of Gal-8, T cell infiltration was associated with a better prognosis. However, this association was absent in tumors that highly expressed Gal-8. MDSCs were ranked among the top Gal-8-associated immunosuppressive cell types that may be associated with T cell exclusion (Figure 1D). To explore the role of Gal-8 in MDSC, we used the TIMER 2.0 algorithm to calculate the immune infiltrations and performed Pearson's correlation analysis between the level of MDSC infiltration and LGALS8 expression based on The Cancer Genome Atlas (TCGA) datasets.[32] The study revealed positive correlations in various cancer types, including adenoid cystic carcinoma, skin cutaneous melanoma (Figure 1E), esophageal cancer, kidney renal papillary cell carcinoma, liver hepatocellular carcinoma, and uterine carcinosarcoma (Figure S1B).

Gal-8 bound to soluble and membrane LILRB4

We attempted to determine whether Gal-8 regulates immune cell function by binding to immune checkpoint membrane proteins to identify further the MDSC subpopulation affected by Gal-8. Among the receptors we tested, strong interactions were observed between Gal-8 and LILRB4 (Figure 1F). We confirmed the presence and strength of this binding using various methods. Immunofluorescence labeling of Gal-8 overexpressed in cells displayed a cytoplasmic punctate-like distribution, as shown in Figure 1G. However, in cells coexpressing LILRB4, the distribution of Gal-8 drastically changed to a pattern similar to that of LILRB4 (Figures 1G and S1C). The coimmunoprecipitation assay also confirmed the interaction between these proteins in the cells (Figure 1H). We then characterized the binding affinity between Gal-8 and LILRB4 using the biolayer interferometry (BLI) assay and ELISA. The binding affinity between Gal-8 and LILRB4 (K_D = 1.02 μM) (Figure 1I) was several-fold higher than that of PD-1/PD-L1 (varied between 7.2 and 8.2 μM, depending on assays).[33] The half-maximal effective concentration (EC_{50}) of Gal-8 in the ELISA binding assay was 1.38 μg/mL with R^2 of 0.994 (Figure S1D). Crosslinking of LILRB4 and Gal-8 resulted in an abundant formation of a larger molecular weight (corresponding to the molecular weight of a polymer formed by two protein monomers in a 1:1 ratio) complex (Figure S1E).

Figure 1. Gal-8 was associated with myeloid cell-mediated immune suppression in the tumor microenvironment and binds soluble and membrane LILRB4

(A) Framework diagram of this research.

(B) Venn diagram demonstrating Gal-8 with a specific expression pattern.

(C) Analysis with the TIDE algorithm shows that LGALS8 plays an important role in T cell dysfunction in the tumor microenvironment. The *Z* score indicates the interaction term in the Cox proportional hazards model and represents the risk coefficient of LGALS8 expression level and T cell dysfunction. The p value represents the significance of Gal-8 as a risk coefficient.

(D) The LGALS8 gene expression value in T cell exclusion signatures calculated with the TIDE algorithm. The association score (*Z* score) of T cell exclusion signatures evaluates how LGALS8 associates with immunosuppressive cell types that drive T cell exclusion.

(E) The TIMER 2.0 algorithm was used to calculate the MDSC fraction and correlation with LGALS8 expression in the indicated types of tumors from the TCGA dataset. Rho and p values are as shown.

(F) ELISA screening of potential immune checkpoint receptors revealed LILRB4 as a Gal-8 interactor.

(G) Intracellular localization of LILRB4 and Gal-8 proteins by fluorescence microscopy. Coexpression with LILRB4 colocalized the Gal-8 protein with LILRB4 at the cell membrane, whereas overexpression alone localized the Gal-8 protein within the cytoplasm. Scale bar, 10 μm.

(H) Immune blotting of coimmunoprecipitation of FLAG-tagged Gal-8 and hemagglutinin (HA)-tagged LILRB4.

(I) BLI assay showing the association-disassociation curve between Gal-8 and LILRB4. The kinetics constants are as follows: kon = 1.29×10^5(1/ms); koff = 1.31×10^{-1}(1/s); K_D = 1.02 μM.

See also Figure S1 and Table S1.

Table 1. Categories of expression patterns of galectins

Names	Total	Elements
Cancer expression, immune privilege associated, and membrane expression	1	LGALS8
Cancer expression and membrane expression	1	LGALS3
Immune privilege associated	3	LGALS14, LGALS13, LGALS16
Membrane expression	1	LGALS4
Cancer expression	4	LGALS9, LGALSL, LGALS1, LGALS2

Gal-8 induced M-MDSC expansion from monocytes

To investigate the cytological function of Gal-8, we first confirmed the binding of Gal-8 to LILRB4 expressed on the HEK293 cell surface (Figure 2A). LILRB4 in immune cells is expressed mainly in monocytic cells, including normal monocytes and plasmacytoid dendritic cells (DCs).[21] Consistent with the potential myeloid-regulating ability of Gal-8, LILRB4 has been reported to induce the tolerance of DCs and expansion of M-MDSCs.[21,23] Therefore, we isolated $CD14^+$ cells from peripheral blood mononuclear cells (PBMCs), treated them with Gal-8, and performed a transcriptome sequencing analysis, an ELISA assay of secreted cytokines, and a T cell proliferation assay (Figure 2B). The transcriptome analysis demonstrated a clear difference in the gene expression patterns between the two groups of $CD14^+$ cells (Figure 2C). Among the most significantly upregulated genes, C300e, IL-6, and MMP8 were reported to be critical for MDSC function, and S100A8/9/12, FCN1, and VCAN were reported as markers of MDSC phenotypes (Figure 2D). Many other genes associated with MDSC functions and induction were upregulated, including CXCL1/2/5, CCL2/7, C3, MMP14, FPR1, IL-1A, MERTK, APQ9, and IL-10 (Table S2). HLA-DR, a negative marker of MDSC, as well as genes negatively related to MDSC accumulation and expansion, such as MMP12, RSAD2, LIPA, STAT1, and ECM1, were significantly downregulated (Figure 2D). Other downregulated genes were related to the DC and macrophage immune response and T cell activation, such as CD1a/b/c and CCL17 (Table S3). We further performed gene set enrichment analysis (GSEA) to investigate monocyte signatures in PBMCs treated with or without Gal-8 (Figure 2E). As a result, we found that a group of gene sets clustered in specific monocyte phenotypes were significantly enriched in Gal-8-treated cells. Such phenotypes included tumor-exposed monocytes (tumor monocyte or spleen monocyte of tumor-bearing mouse), M-MDSC-like monocytes (Ly-6C-high monocyte), and MDSCs with stronger suppressive functions (HDC-KO MDSC) (Figure 2E). Genomic Spatial Event (GSE) numbers and whole names of these enriched gene sets are listed in Table S4. In addition, Gal-8 treatment correlated with the negative regulation of defense response (Figure S2A) and the downregulation of T cell infiltration in tumors (Figure S2B). We also analyzed the morphological changes and cytokine secretion of $CD14^+$ monocytes following Gal-8 treatment. As shown in Figure S2C, cells without Gal-8 treatment appeared rounder and more tightly packed. Consistently, other researchers reported the rounding of spindle-like morphology when the immunosuppressive properties of human-derived macrophages are diminished.[34] The IL-10 levels in the supernatant of $CD14^+$ cells treated with Gal-8 were significantly higher than those in the control group (Figure S2D).

Considering the presence of a discovered ligand, APOE, for LILRB4,[19] it is necessary to clarify the differences between these two ligands regarding binding and function. In the ELISA assay, when an increased concentration of APOE was added, the binding of Gal-8 to LILRB4 was unaffected (Figure S2E), suggesting that Gal-8 and APOE bind LILRB4 at different conformational regions or in different manners. Accordingly, we explored the effect of Gal-8 on the M-MDSC phenotype. For human-derived PBMCs, we added granulocyte-macrophage colony-stimulating factor (GM-CSF) to maintain monocytes *in vitro* without adding other cytokines customarily used to induce MDSC. We found that Gal-8 adequately induced M-MDSC expansion under this condition. In contrast to Gal-8, APOE had no amplification effect on M-MDSCs (Figure 2F). Moreover, the T cell proliferation assay proved that the Gal-8-induced MDSCs were functionally competent (Figure 2G). Notably, Gal-8 was added only to isolated $CD14^+$ cells for 3 days but not to cocultured cells. As the concentration of Gal-8 increased, the suppression of T cells by the treated $CD14^+$ cells became stronger.

Gal-8-LILRB4 interaction activated signal transducer and activator of transcription 3 (STAT3) and inhibited nuclear factor κB (NF-κB) through SHP-1

We further explored the effect of Gal-8 binding to LILRB4 on the downstream signaling factors. The THP-1 cell line expresses high-level LILRB4, and is often used in monocytic studies.[35] To better demonstrate the function of Gal-8-LILRB4, an LILRB4-knockdown (KD) THP-1 cell line was constructed using small hairpin RNA (shRNA) lentivirus (THP-1 LILRB4 KD), and cargo lentivirus was used to build a control cell line (THP-1 Vector). The intracellular domain of LILRB4 contains three ITIMs that were reported to recruit Src homology 2 (SH2)-containing tyrosine phosphatases (SHPs) and SH2 domain-containing inositol phosphatase (SHIP) to transduce inhibitory signals.[36] Gal-8 was added to THP-1 (Vector or LILRB4 KD) cells, and phosphorylation of downstream phosphatases was detected. We found that SHP-1 phosphorylation (and not SHP-2 or SHIP-1) elevated in a concentration-dependent manner in THP-1 Vector cells but not in LILRB4-KD THP-1 cells (Figure 3A), which agreed with a previous report on the ability of LILRB4 to promote SHP-1 phosphorylation.[37]

Furthermore, we detected substantial NF-κB inhibition upon Gal-8-LILRB4 interaction (Figure 3B), possibly because of the specific effect on SHP-1. In addition, STAT3 was reported to be activated by SHP-1[38] and contribute to MDSC induction.[39] Accordingly, STAT3 phosphorylation was found to be activated by Gal-8 (Figure 3B). The same phenomenon was observed in another monocyte cell line, MV411, which highly expressed LILRB4 (Figure 3C). In LILRB4 KD cells, the NF-κB phosphorylation level was not inhibited by Gal-8, and STAT3 phosphorylation was weaker (Figure S3A), indicating that the downstream signaling was LILRB4 dependent. It has been found that

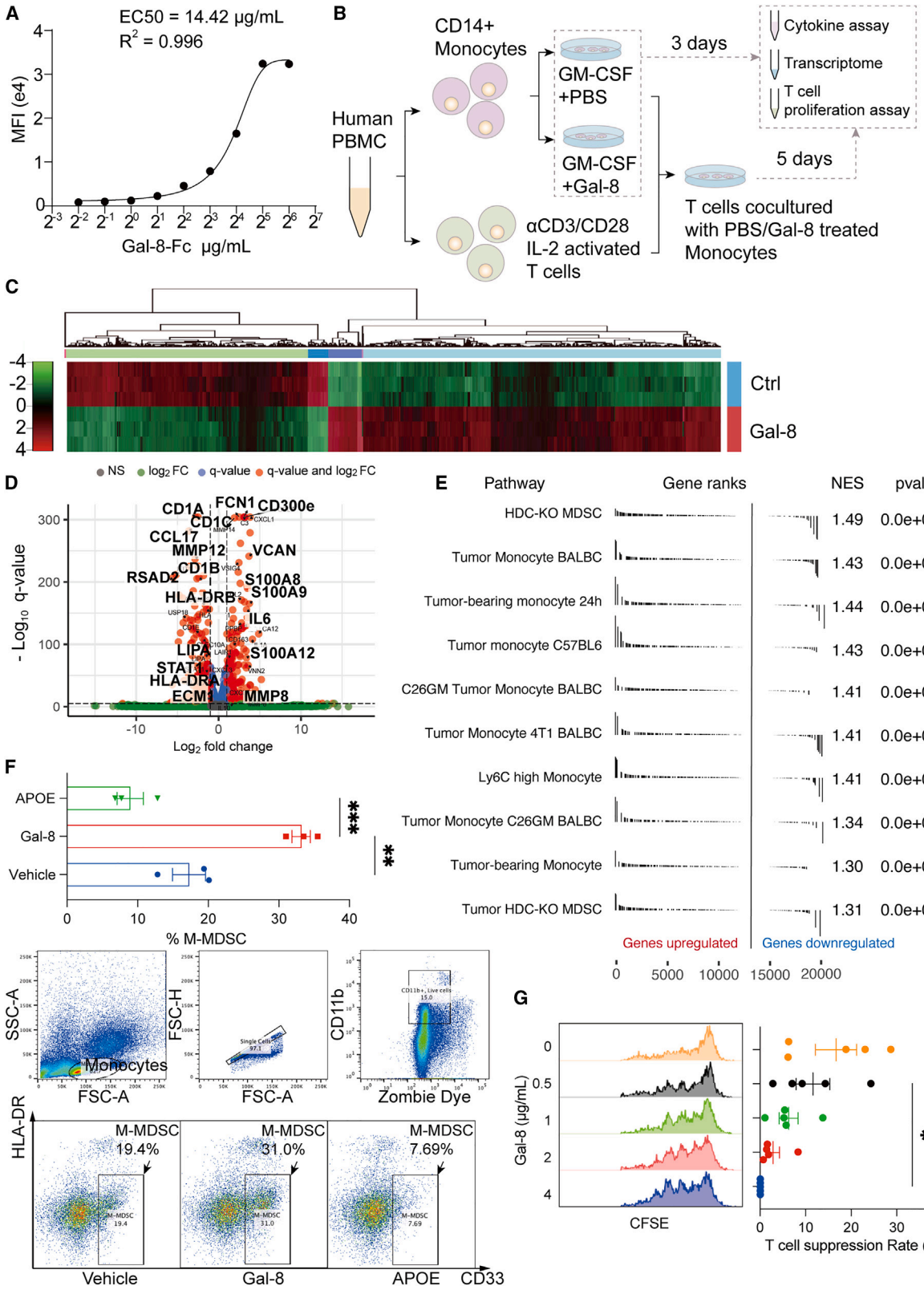

(legend on next page)

SHP-1, SHP-2, and SHIP may adapt LILRB4 ITIMs to different downstream signaling pathways. The Gal-8/LILRB4/SHP-1 axis displayed no effect on ERK1/2 signaling (Figure S3B), although LILRB4 in lung cancer cells may activate ERK1/2 through SHP-2 and SHIP-1.[40] Similarly, the Gal-8/LILRB4/SHP-1 axis did not affect Akt phosphorylation (Figure S3B), which may result from LILRB4 recruiting SHP-2 in certain lymphoma cells.[41]

APOE-LILRB4 interaction was reported to activate NF-κB through SHP-2 in AML cells, with decreased NF-κB nuclear translocation in LILRB4 KD THP-1 cells.[19] We detected NF-κB and STAT3 after separating the cytoplasmic and nuclear fractions. The result was consistent with the report that NF-κB in the nuclear protein pool decreased in LILRB4 KD cells. Our findings revealed that phosphorylated NF-κB was vastly enhanced without LILRB4, and the phosphorylation of STAT3 was lower in LILRB4 KD cells than in control cells (Figure 3D). The regulation of STAT3 and NF-κB was investigated further in isolated $CD14^+$ cells (Figure 3E).

SHP-1-STAT3-S100A8/9 as a downstream pathway of Gal-8-LILRB4 interaction

In Figures 3B and 3C, altered phosphorylation of STAT3 and NF-κB showed different temporal properties; in detail, the increase in STAT3 phosphorylation was more pronounced at 24 h, whereas the inhibition of NF-κB phosphorylation was more pronounced after a more extended period. We thus infer that the phosphorylation from SHP-1 to STAT3 is regulated more directly and to NF-κB indirectly. We first clarified that the altered STAT3 phosphorylation brought about by Gal-8-LILRB4 signaling occurs mainly at tyrosine 705 but not serine 727 (Figures S3A and S3C). In addition, TPI, a selective inhibitor of SHP-1, successfully blocked STAT3 phosphorylation (Figure S3C), supporting the function of the SHP-1-STAT3 pathway in monocytes.

Both S100A8/9 were detected to be altered consistently with STAT3 activation (Figure 3F). They were considered critical factors in STAT3 signaling during MDSC induction and as markers of human M-MDSC.[42,43] The suppressor of cytokine signaling (SOCS3) is a negative feedback regulator of STAT3. It has been reported that NF-κB regulates SOCS3 expression, causing STAT3 inhibition.[44] In our assay, SCOS3 did not decrease in parallel with STAT3 activation, suggesting that it may not be responsible for the altered STAT3 phosphorylation (Figure 3F).

Gal-8-LILRB4-SHP-1 inhibited ADAM17 through TRAF6-NF-κB

SHP-1 was reported to inhibit TRAF6 ubiquitination by dephosphorylating TRAF6,[45] and TRAF6 ubiquitination was thought to activate NF-κB.[46,47] Therefore, we pulled down TRAF6 with an anti-TRAF6 antibody and detected ubiquitination with immune blotting. In LILRB4 KD cells, ubiquitination of TRAF6 was more robust, and phosphorylation of NF-κB was promoted (Figure 3G). In wild-type (WT) THP-1 cells, Gal-8 treatment downregulated the ubiquitination of TRAF6 (Figure 3H). In THP-1 (NF-κB) reporter cells cocultured with HEK293 cells overexpressing Gal-8, NF-κB signaling was also inhibited, compared to that in cells cocultured with Vector cells (Figure 3I).

As a well-addressed yet complex transcription factor, NF-κB controls the transcription of various target genes. Through exploration of the literature, we identified an NF-κB regulating factor, ADAM17,[48] which was closely related to the IL-6 signaling.[49] ADAM17 was believed to be involved in the immune regulation.[50] The membrane expression of ADAM17 in THP-1 cells decreased with increased Gal-8, whereas the KD of LILRB4 increased ADAM17 expression (Figure 3J). Consistent with whole-cell lysate expression, the surface level of ADAM17 was downregulated by Gal-8 (Figure S3D) in THP-1 cells, similar to that in human monocytes sorted from PBMCs (Figure S3E). ADAM17 was thought to cleave membrane proteins into soluble forms, thus reducing their membrane expression.[49] We detected IL-6R membrane expression and found it increased with Gal-8 treatment (Figure S3F). Consistently, soluble IL-6R levels decreased in the culture medium (Figure S3G). Hypothetically, the upregulation of membrane IL-6R empowers IL-6 signal transduction, and reduced sIL-6R strengthens this effect, fueling STAT3 activation and MDSC expansion. Meanwhile, PD-L1[51] and CD163,[52] also known to be cleaved by ADAM17, were not notably affected either in immune blotting (Figure S3H) or in fragment crystallizable of IgG (FC) assays (Figures S3I and S3J).

Gal-8 and LILRB4 interaction promoted tumor growth *in vivo*

Before performing the *in vivo* experiment, we confirmed the binding of mouse LILRB4 and human Gal-8 by ELISA (Figure 4A). With the CRISPR-Cas9 technique, the lilrb4 knockout (HE) mouse strain was built from C57BL/6Smoc mice. Wild-type C57BL/6Smoc mice were used as controls. B16, a melanoma cell line derived from C56BL/6 mice, was transfected with plasmids to construct a stable cell line overexpressing human Gal-8

Figure 2. Gal-8 binds LILRB4 to induce MDSC expansion

(A) Affinity of Fc-tagged Gal-8 protein and HEK293 cell-expressed LILRB4 represented by EC_{50} of flow cytometry assay.

(B) Schematic illustration of experiment design.

(C) Heatmap of the transcriptome sequencing data of $CD14^+$ cells. Each group contains 3 biological replicates.

(D) Volcano plot of the transcriptome sequencing data. The analysis was performed based on the false discovery rate q value. The top-ranked genes were strongly correlated with MDSC phenotype and function.

(E) GSEA showing RNA sequencing–based monocyte signature evaluated in the context of gene sets representative of immune functions.

(F) Flow cytometry assay detecting the percentage of M-MDSC with or without Gal-8 or APOE treatment. $CD11b^+$, $CD33^+$, HLA-$DR^{low/-}$, and live monocytes were defined as M-MDSCs. Statistical results were obtained from 3 biological replicates and represented as mean ± SEM.

(G) T cell proliferation assay showing that monocytes exposed to Gal-8 inhibited T cell function in a concentration-dependent manner. The T cell suppression rate represents the percentage of decreased proliferation rate compared to the control group (whose suppression rate was zero). Data were obtained from biological replicates and represented as mean ± SEM.

See also Figure S2 and Tables S2, S3, and S4.

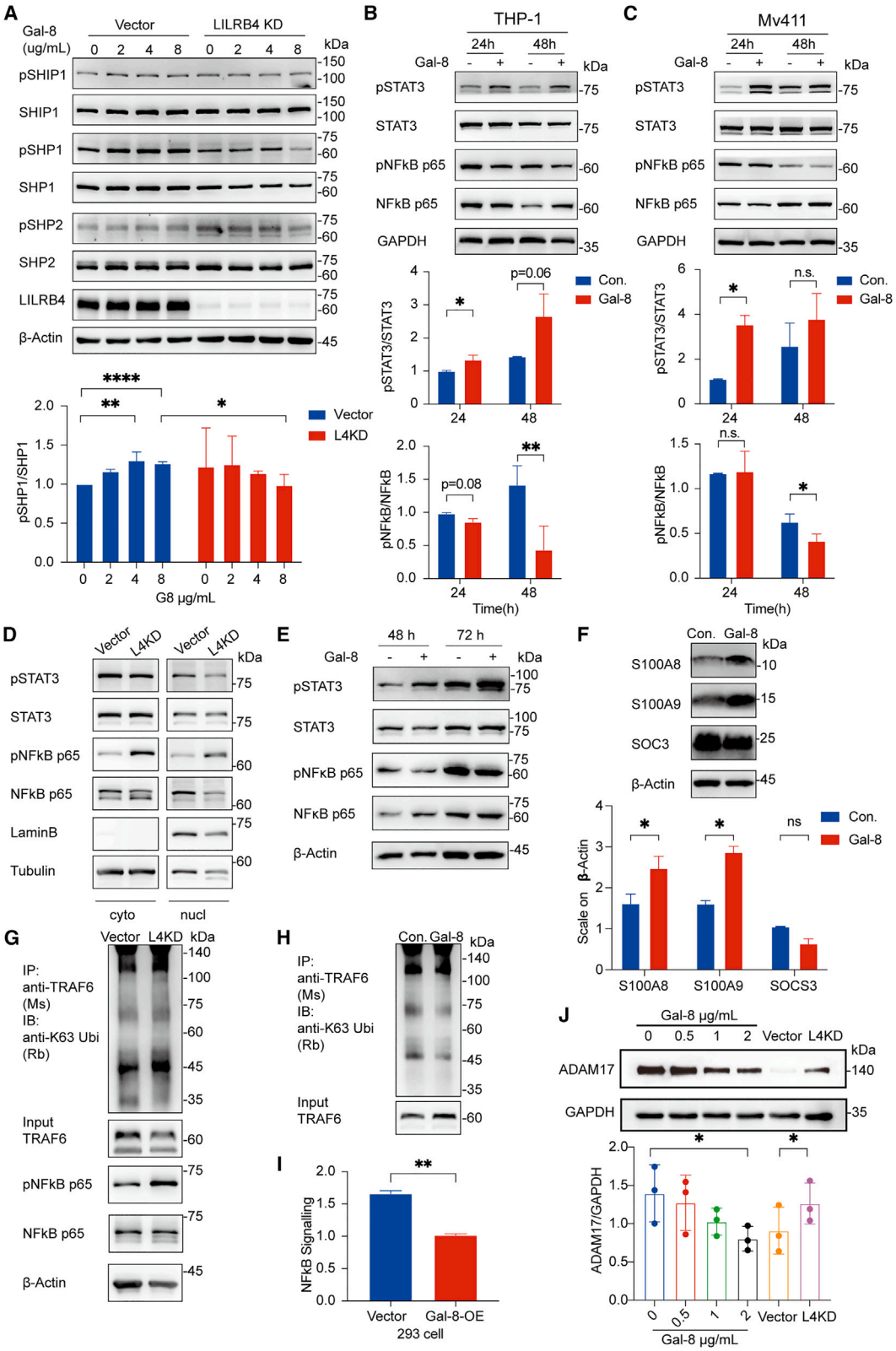

(legend on next page)

(HuGal-8-OE, referred as Gal-8-OE below) (Figure S4A). Vector plasmids were used to construct control cell lines (Vector). An antibody that binds to both human and mouse Gal-8 was used in immunoblotting detection, showing that endogenously expressed Gal-8 was rather low compared to the overexpressed protein levels. The MC38 cell line was also used to construct a stably transfected cell line overexpressing Gal-8 and was used in later experiments (Figure S4B).

Cells were injected subcutaneously into lilrb4 knockout (lilrb4-KO) and WT mice (Figure 4B). Subcutaneous tumors were detectable in most mice 9 days postinjection. The size of the tumors was measured every 3 days until the tumor size was not ethically acceptable. Over time, Gal-8-OE tumors grew faster than WT tumors, and in WT mice rather than in lilrb4-KO mice (Figure 4C). After the mice were sacrificed, dissected tumors were photographed *in vivo* and *ex vivo* (Figure 4D). In a different batch of experiments, only mice with tumor volumes exceeding the ethical limit or with ulceration were executed and recorded as dead. Survival curves were calculated for the four groups of mice (Figure 4E).

In the flow cytometry assay to detect MDSCs, M-MDSCs were defined as $CD11b^{+}Ly^{-}6C^{+}Ly\text{-}6G^{-}$ cells, and G-MDSCs as $CD11b^{+}Ly6G^{+}Ly^{-}6C^{-}$ cells (Figure S4C). In tumors isolated from the two groups inoculated with Gal-8-OE cells, the lilrb4-KO group had significantly lower M-MDSC levels than did the WT group (Figure 4F). Splenocytes and PBMCs were also sampled to evaluate the levels of systemic M-MDSCs, and the WT + Gal-8-OE group showed the highest levels of M-MDSCs in both (Figures 4G and 4H). Notably, the M-MDSC level of the WT + Gal-8-OE group was greater than that of the WT + WT group in PBMCs (Figure 4G). In splenocytes, the M-MDSC level in the WT + Gal-8-OE group was higher than in the lilrb4-KO + Gal-8-OE group (Figure 4H). The G-MDSCs showed no significant differences in the four groups, either in the tumor, PBMS, or splenocytes (Figures S4D and S4F).

MDSCs were reported to suppress T cell infiltration and induce Tregs.[53] Using dissected tumor samples, immunohistochemistry (IHC) staining for FoxP3 and CD8 was performed. The results showed that Gal-8 and LILRB4 upregulated Treg levels and downregulated $CD8^{+}$ T cell infiltration in both B16 tumors (Figures 4I and 4J). Representative views of FOXP3 and CD8 IHC staining were shown in Figures 4K and 4L, respectively. Mechanistic studies revealed two downstream pathways of LILRB4 in regulating monocyte activity (Figure 4M).

Anti-LILRB4 monoclonal antibodies that bound to a specific epitope blocked Gal-8-LILRB4 interaction and tumor growth

With a functional basis for ligand-receptor activity, we attempted to develop antibody drugs that could block Gal-8-LILRB4 binding. Mice were immunized with human LILRB4 extracellular domain recombinant protein, and their splenocytes were isolated and fused with hybridoma cells, which were then screened to produce monoclonal anti-LILRB4 antibodies (Figure 5A). After validation, 24 monoclonal antibodies were identified to specifically bind to the recombinant LILRB4 protein (Figure S5A). We then performed epitope binning on these antibodies and identified four different bins (Figure 5B). BLI analysis revealed that clone 3–11, 4–25, and 4–39 competitively bound to the LILRB4 protein (Figure 5C), while antibodies from other bins did not (Figure S5B). Since competitive antibodies bind to the same or similar epitopes, antibodies from each group were picked out for the ELISA assay to see whether they could block the binding of Gal-8 and LILRB4. The results showed that clone 4–25 from bin 4 had a concentration-dependent blocking effect (Figure S5C). Afterward, all of the antibodies of bin 4 were detected at more concentrations for concentration-dependent blocking effects (Figure 5D). The half-maximal inhibitory concentration (IC_{50}) of the three clones were 0.823 (3–11), 0.013 (4–25), and 2.349 (4–39) μg/mL, respectively. For clone 3–11 and 4–25 with lower IC_{50}, we tested their binding affinity to LILRB4 protein using the BLI system, and the results were 3.97×10^{-10} M and 7.11×10^{-9} M, respectively (Figure 5E).

To determine the epitope of bin 4 antibodies, we designed 11 polypeptides (namely, P1−P11) with a length of 27 amino acids and overlapping ends according to the sequence of the extracellular domain of LILRB4 (Table S5). We detected the binding of the antibodies to these peptides by ELISA. This method could detect the ability of the antibodies to bind to linear epitopes, and antibodies bound to different peptides had different epitopes, such as clones 4–13 and 4–25 (Figure S5D), and also clones 4–25 and 3–11 bound to polypeptide P10 (Figure 5F). Since the binding signal of clones 3–11 is stronger, we next used clones 3–11 to confirm further which amino acid residues on P10 are key binding sites. We obtained 27 different mutant peptides by mutating 27 amino acid residues into alanine, an amino acid with poor polarity, and then determine which mutations significantly affected the antibody binding to these peptides (Table S6). The results showed

Figure 3. Gal-8-LILRB4 interaction activates STAT3 and inhibits NF-κB pathway

(A) Immune blotting of 3 potential protein tyrosine phosphatases (PTPs) downstream of LILRB4. Among the 3 PTPs, the phosphorylation level of SHP1 was significantly affected by Gal-8. The statistical plot shows the pSHP1/SHP ratio.

(B and C) Immune blotting demonstrates the phosphorylation level of NF-κB and STAT3 with or without Gal-8 treatment in THP-1 (B) and MV411(C) cells.

(D) Immune blotting of nuclear and extranuclear proteins of Vector and LILRB4 KD THP-1 cells.

(E) Immune blotting of human $CD14^{+}$ cells treated with or without Gal-8 for 48 or 72 h. The results were constant with what was observed in THP-1 and MV411 cell lines.

(F) Immune blotting of S100A8/9 and SOCS3 in human $CD14^{+}$ cells treated with or without Gal-8.

(G and H) Immune blotting of TRAF6 ubiquitination in THP-1 cells with or without LILRB4 KD (G) and with or without Gal-8 treatment (H). The immune blotting was detected with an anti-K63 Ubi antibody.

(I) NF-κB reporter gene signal intensity in THP-1 cells cocultured with Gal-8-overexpressing HEK293 cells or control HEK293 cells for 3 days before reporter signals were detected.

(J) Immune blotting of ADAM17 expression alteration in THP-1 cells treated with different concentrations of Gal-8 and in Vector and LILRB4-KD THP-1 cells. Of all the statistical analysis of immune blotting results, data were obtained from 3 biological replicates and represented as mean ± SEM.

See also Figure S3.

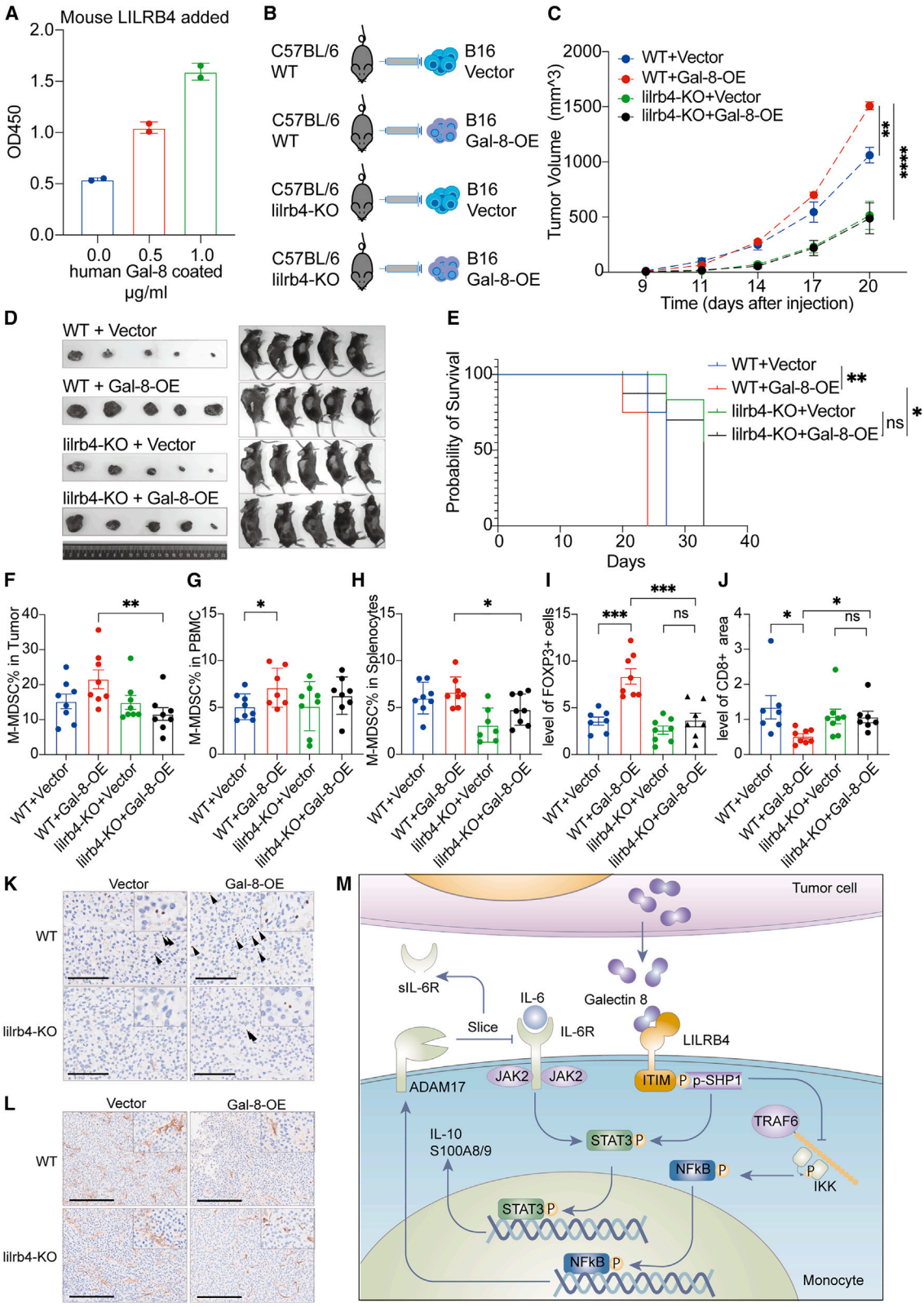

(legend on next page)

that the amino acid mutation between PHE190 and CYS195 influenced the binding strength, suggesting that this may be the binding epitope for clones 3–11, as shown in Figure 5G.

Before testing the biological function of the antibody, we clarified that the antibodies bound to the LILRB4 protein expressed on the cell surface using THP-1 cells (Figure 5H). Both clones 3–11 and 4−25 decreased MDSC expansion induced by Gal-8, compared to mouse IgG (Figure 5I). To avoid interference of the Fc segment with cell signaling *in vitro*, we digested antibodies 4–25 with papain and purified the Fab segment (Figure S5E). $CD14^+$ cells were sorted from human PBMCs and exposed to Gal-8 treatment, and the phosphorylation level of STAT3 was reduced with increasing concentrations of the 4–25 Fab protein. In contrast, that of NF-κB was increased, reversing the effects of Gal-8 (Figure 5J). The morphological changes of $CD14^+$ monocytes treated with Gal-8 were also reversed by the 4–25 Fab protein (Figure S5F). Consistent with the above results, the 4–25 antibody inhibited tumor growth *in vivo* compared to control IgG (Figure 5K). In the syngeneic model, B16 cells transfected with human Gal-8 were injected subcutaneously into humanized LILRB4 (hLILRB4) mice. The Gal-8-OE B16 cells expressed a comparable level of Gal-8 to the human melanoma cell line, A375 (Figure S5G), and *in vivo* expression of Gal-8 by inoculated tumors was later compared with human melanoma tissues. The antibody-blocking mechanism was displayed graphically (Figure 5L).

Anti-Gal-8 monoclonal antibody that blocked Gal-8-LILRB4 interaction had a similar effect on tumor growth with anti-LILRB4 antibody

Gal-8, as a functional ligand of LILRB4, is of potential value as a therapeutic target, and the function of anti-Gal-8 antibodies could support the demonstration of Gal-8-LILRB4 interaction. Mice were cross-immunized by human and cynomolgus antigens to produce anti-Gal-8 antibodies. Through screening, we identified 34 different strains of antibodies with high affinity to both human and cynomolgus Gal-8 (Figure 6A), performed epitope binning using the BLI system (Figure 6B), and selected antibodies with different epitopes for ELISA blocking experiments (Figure 6C). As a result, strain numbers 26 and 34 (clone names A237 and A269) showed a stronger capacity to block the binding of Gal-8 and LILRB4. To compare the blocking ability of the two clones in a dynamic environment, we performed blocking detection with the BLI system. Specifically, the A269 or A237 antibody that was immobilized on the probe first bound the Gal-8 protein (step 1 in Figure 6D), and the probe was subsequently placed in a solution of recombinant LILRB4 protein. The LILRB4 protein could no longer bind to Gal-8 bound to A269 but continued to bind to A237-bound Gal-8 (step 2 in Figure 6D). This phenomenon may be due to the difference in affinity between the two antibodies (Figures 6E and 6F). In addition, we performed dot blotting to detect their binding ability to mouse Gal-8, using lysates of B16 cells overexpressing mouse Gal-8. Both clones showed no significant binding to mouse Gal-8 (Figure S6A). In the MDSC induction assay, the anti-Gal-8 antibody functionally blocked the induction of MDSC by Gal-8 (Figure S6B).

To select suitable human-derived tumors for the construction of *in vivo* models, we stained cell-expressed Gal-8 proteins in different cell lines with A269 antibody and detected them by flow cytometry (Figure S6C), consistent with Gal-8 mRNA level indicated in the Cancer Cell Line Encyclopedia database (Figure S6D). Because galectins were reported to be secreted into the extracellular space,[10] we detected Gal-8 expression in the cell supernatant using an in-house-developed ELISA kit. Cell supernatants were obtained from T25 cell culture flasks. Because the number of both cells was not controlled, the results indicated only the presence of secreted Gal-8 in the supernatant but not the level of secreted Gal-8 (Figure S6E). These cells were used to construct *in vivo* therapeutic models.

A375 and HCT116 cells were mixed with human PBMCs at a 4:1 ratio and injected subcutaneously into the NCG mouse. When the size of the subcutaneous tumors in mice was approximately 80–100 mm^3, the mice were evenly divided into 3 groups (n = 6 for each group) and were injected intraperitoneally with vehicle solution, anti-Gal-8 antibody (clone A269) and anti-LILRB4 antibody (clones 4–25) (Figures 6G–6J). In these models, the anti-Gal-8 and anti-LILRB4 antibodies showed comparable therapeutic effects, and their inhibition of tumor volume was more potent for the A375 tumors. Notably, A375 not only expressed a higher level of Gal-8 but was also reported to be used in coculture with $CD14^+$ monocytes to construct an *in vitro* M-MDSC model,[54] suggesting that there is a consistency between the therapeutic effect of the antibody and the ability to induce M-MDSC.

Figure 4. Gal-8 and LILRB4 interaction alters the microenvironment and promotes tumor growth *in vivo*

(A) ELISA results detecting binding capacity of mouse LILRB4 and human Gal-8 proteins. Human Gal-8 was coated on ELISA plates and incubated with murine LILRB4-Fc protein.

(B) Strategic diagram of tumor transplant mice model (n = 8).

(C) B16 tumor volume.

(D) Photograph of B16 tumor *in vivo* and *ex vivo*.

(E) Survival curves of tumor-bearing mice.

(F) Tumor-infiltrating M-MDSC level detected by flow cytometry assay. The proportion of M-MDSC to $CD45^+CD11b^+$ cells was statistically compared.

(G and H) Ratio of M-MDSCs in the peripheral blood (G) and spleens (H) of mice bearing B16 tumors.

(I–L) Tumor infiltrating $FOXP3^+$ Tregs and $CD8^+$ T cells in tumor IHC assay. (I) Under a 40× objective lens, 5 fields of view were randomly captured on each tumor sample slide, and the number of $FOXP3^+$ cells in these fields of view was counted and averaged, which was recorded as the $FOXP3^+$ cell level of that sample. (J) Five 20× fields of view were randomly captured on each slide, and the area of positive staining was calculated using ImageJ and recorded as the $CD8^+$ area level for that sample. The $FOXP3^+$ and $CD8^+$ level was statistically compared for each group of 8 samples. All of the statistical data mentioned above was represented as mean ± SEM. (K) $FOXP3^+$ cells stained in B16 tumor (scale bar, 100 μm). (L) $CD8^+$ cells stained in B16 tumor (scale bar, 250 μm).

(M) Mechanistic diagram demonstrating downstream signaling of Gal-8-LILRB4.

See also Figure S4.

CellPress
OPEN ACCESS

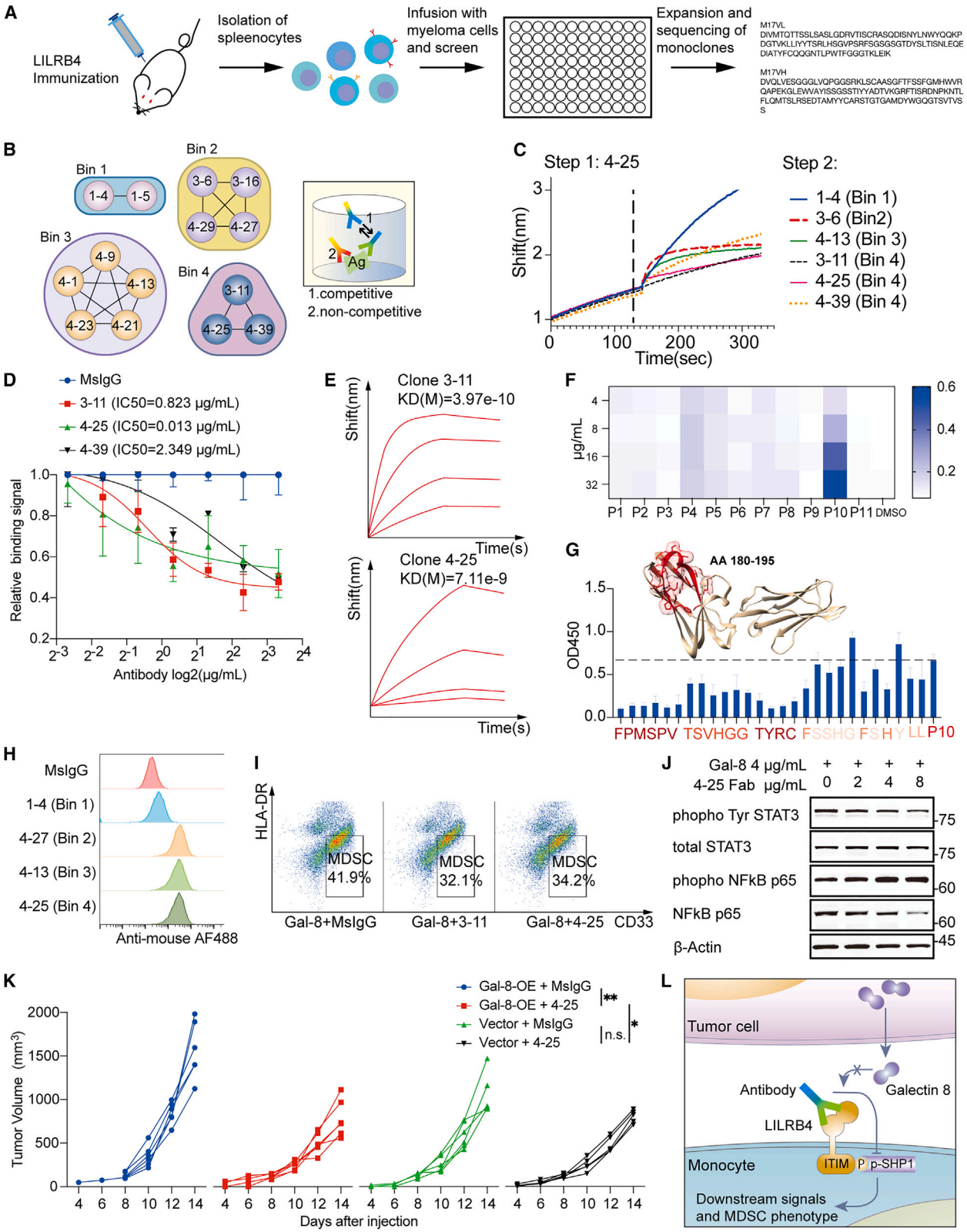

(legend on next page)

We performed IHC staining to detect Gal-8 expression levels in melanomas from 46 patients on tissue microarrays. By scoring the area and intensity of positivity separately and calculating the total score, we classified the expression of Gal-8 in melanoma tissues into four levels (Figure 6K). Over 70% of melanoma samples had medium to strong Gal-8 expression (Figure 6L). We also performed IHC staining for Gal-8 in tumors dissected from the *in vivo* models. The Gal-8-OE tumor models used in this study showed comparable levels of Gal-8 expression to those found in human tumor tissues (Figure S6F).

We further explored the therapeutic effect of anti-Gal-8 antibody in combination with PD-L1 blockade. The MC38 is a murine-derived colon cancer cell line often used to construct mouse tumor models sensitive to the anti-PD-L1 treatment.[55] In our *in vivo* model built with C57BL/6Smoc WT mice and MC38 cells overexpressing Gal-8, the anti-Gal-8 antibody (A269) inhibited tumor growth alone, and it further reduced the tumor volume based on anti-PD-L1 antibody treatment (Figures 6M and 6N). Consistently, the Gal-8 antibody resulted in increased $CD8^+$ cell infiltration and decreased $FOXP3^+$ cell infiltration (Figures S6G–S6I). Regarding body weight, mice in the antibody-treated group had higher body weights than the vehicle control group, showing no apparent toxicity (Figure S6J).

DISCUSSION

Increasing evidence suggests that the galectin family correlates with tumor progression and immune escape. Among them, Gal-8 has a distinctive expression pattern, although it remains understudied and highly controversial in tumor immune regulation. We noted some prominent associations by analyzing databases and felt a strong need for an in-depth study of Gal-8.

We identified Gal-8 as an LILRB4 ligand that induces MDSC expansion. Gal-8 correlates with poor prognosis in patients with cytotoxic T lymphocyte tumor infiltration, indicating that Gal-8 may induce immunosuppression in the tumor microenvironment. The regulation of immune function by Gal-8 under physiological conditions is quite complicated. Interestingly, previous studies have suggested that Gal-8 has an activating effect on resting immune cells and an inhibitory effect on activated immune cells.[16] Moreover, Gal-8 exhibits immunosuppressive properties in tumor and autoimmune disorders, reflecting both temporal and spatial functional differences. It has been reported that Gal-8 induces Treg only at inflammatory sites, without systemic effects on resting CD4.[16] This suggests that Gal-8 needs some important mediators at the site of inflammatory, such as LILRB4-expressing antigen-presenting cells (APC)s, and consequently induces MDSCs to exert immunosuppressive effects. These features can be cleverly exploited by tumors, allowing Gal-8, which is highly expressed in tumors, to be a factor that induces immunosuppression in the tumor microenvironment. The interaction between Gal-8 and LILRB4 was confirmed by various methods, such as their ability to induce the suppressive phenotype of monocytes. *In vivo* studies have emphasized their role in mediating immune suppression and tumor progression.

STAT3 was reported to be phosphorylated during the activation of immature monocytes, which is thought to be a crucial step toward MDSC expansion in the two-stage model proposed by Gabrilovich et al.[56] In this model, the activation of immature myeloid cells by STAT3 precedes the accumulation of suppressive myeloid cells, comprising two indispensable stages that mutually contribute to MDSC expansion. Based on collective evidence, the activation of STAT3 through LILRB4 proves that Gal-8 is an unknown yet crucial myeloid suppressor. In contrast, decreased NF-κB phosphorylation was induced via the LILRB4-SHP1-TRAF6 pathway. Although NF-κB was reported to mediate immune suppression of MDSC,[57] its status during the induction of MDSC remained unclear. In macrophages, NF-κB was regarded as an activator of phagocytosis.[58] Therefore, NF-κB inhibition may regulate monocyte suppression, one of the stages of MDSC development.

Mechanistically, we revealed that the ADAM17-IL6R pathway links NF-κB inhibition and STAT3 activation. The collaboration of the STAT3 and NF-κB pathways was assumed to drive cancer by controlling the communication between cancer cells and inflammatory cells.[59] The interaction between the two pathways added complexity to the MDSC expansion process, and researchers have made assumptions supporting a multistage model of the MDSC expansion.[60] These two pathways induced by LILRB4 mutually enhanced MDSC, showing that LILRB4 signaling was involved in multiple stages of MDSC expansion.

In the *in vivo* models, Gal-8-LILRB4 interactions promoted immunosuppression and tumor growth, resulting in a worse

Figure 5. Anti-LILRB4 monoclonal antibodies that bind specific epitopes blocked Gal-8-LILRB4 interaction and tumor growth

(A) The process of producing mouse anti-LILRB4 monoclonal antibodies from hybridoma.

(B) Results of epitope binning and schematic diagram. Antibodies were categorized into 4 bins according to their binding epitope.

(C) Clones 4–25 competed with other bin 4 clones but not clones from other bins to bind LILRB4 antigen in the BLI system. The shift of BLI did not increase when antibodies competed for the same epitope, whereas antibodies binding to a different epitope continued to bind to the antigen, further increasing the shift.

(D) The blocking capacity of bin 4 antibodies represented by ELISA IC_{50}. Statistical results were obtained from 3 replicate wells and represented as mean ± SEM.

(E) The affinity curve of clones 3–11 and 4–15 antibodies detected and analyzed with the BLI system.

(F) ELISA results demonstrating the linear epitope of the clones 3–11 antibody. The clones 3–11 antibody was shown to bind peptide P10 predominantly.

(G) Epitope mapping of clones 3–11 antibody. Mutated amino acid sites with more significant interference on the ELISA binding signal were labeled darker in the figure. These amino acid sites and their binding signals were marked based on the molecular structure of the extracellular domain of LILRB4.

(H) Flow cytometry assay revealed binding to THP-1 cells of the antibodies from different bins.

(I) Flow cytometry assay of M-MDSC. The gating strategy was as described above. Compared with the mouse immunoglobulin G (msIgG), the clones 3–11 and 4–25 antibodies reduced the expansion of MDSC induced by Gal-8.

(J) The Fab segment of clones 4–25 antibody reversed Gal-8-induced STAT3 activation and NF-κB inhibition in $CD14^+$ monocytes.

(K) Clones 4–25 antibody inhibited the growth of Gal-8 overexpressed tumors *in vivo* compared with isotype control.

(L) Mechanism diagram of the blocking effect of anti-LILRB4 antibodies.

See also Figure S5 and Tables S5 and S6.

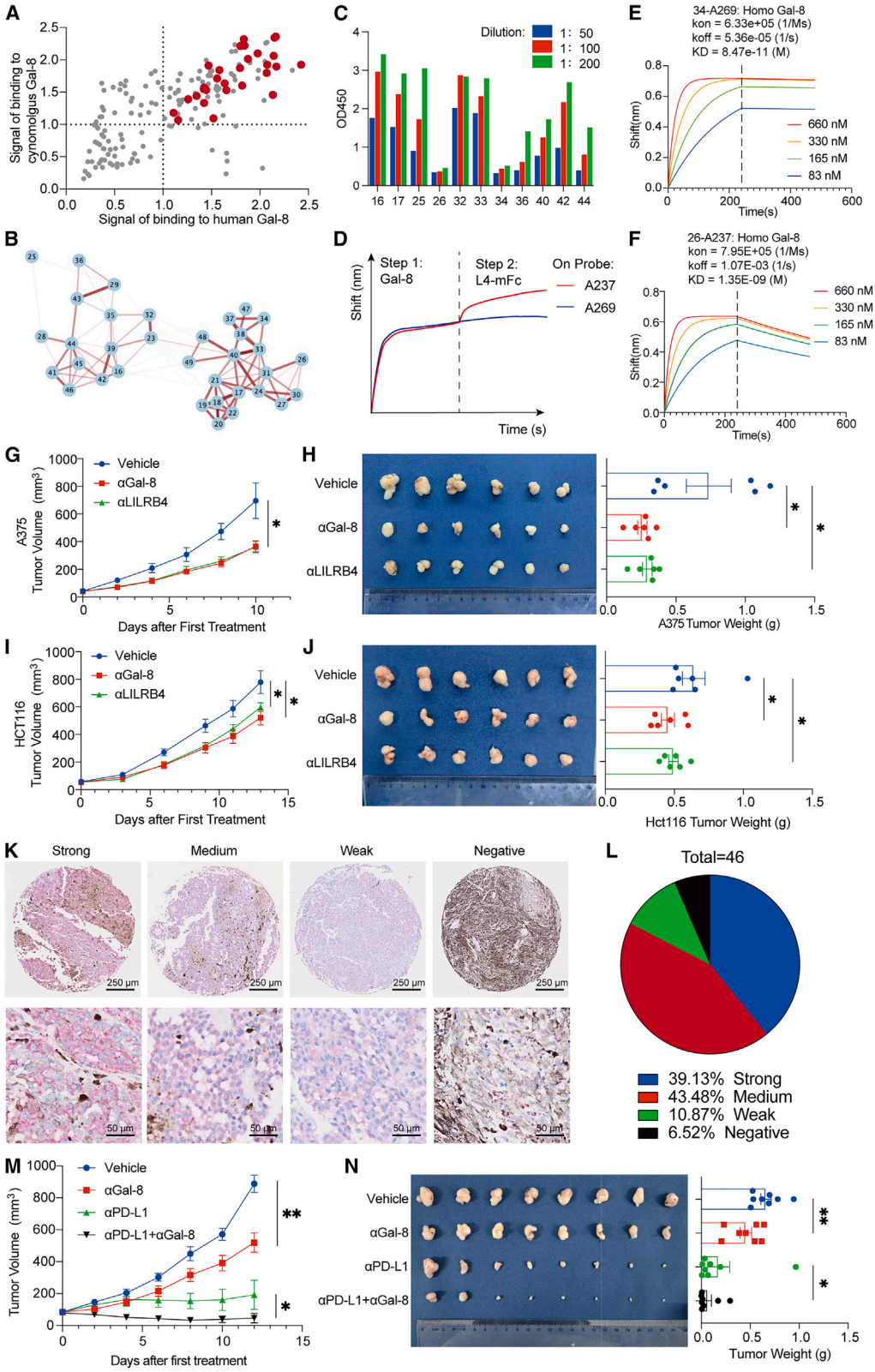

(legend on next page)

prognosis. Interestingly, in detecting M-MDSC in multiple tissues, the M-MDSCs in central immune organs were closely related to the LILRB4 phenotype. In contrast, M-MDSCs in peripheral blood were more susceptible to tumor Gal-8 expression, suggesting a mutual influence of Gal-8 and LILRB4 on the overall immune activity of tumor-bearing mice. On this basis, we developed both anti-LILRB4 and anti-Gal-8 antibodies capable of functionally blocking the ligand–receptor interaction and confirmed antibody therapeutic effects *in vivo*. Animal-generated antibodies bind to numerous sites, possibly leading to different functions. Unlike previous studies of LILRB4 antibodies for treating solid tumors, we clarified the epitopes bound by antibodies with blocking properties, offering the possibility of more efficient early screening of antibody drugs in the early development stage. The discovery of Gal-8 as a functional ligand for LILRB4 also provides potentially valuable CDx criteria for future clinical studies of LILRB4 antibody drugs and new targets for MDSC-targeted drugs. Given its potential clinical value, the binding of Gal-8 and LILRB4 deserves more attention in drug development.

Limitations of the study

Due to the complexity of ligand-receptor interactions, our screening methodology does not allow us to determine whether there will be other ligands with different or the same function for LILRB4 and the effect of the antibodies we developed on them. In terms of MDSC-inducing mechanisms, we identified two pathways and hypothesized their phases of action, but how they determine cell differentiation step by step from multiple levels such as genes and proteins requires further research.

STAR★METHODS

Detailed methods are provided in the online version of this paper and include the following:

- KEY RESOURCES TABLE
- RESOURCE AVAILABILITY
  - Lead contact
  - Materials availability
  - Data and code availability
- EXPERIMENTAL MODEL AND STUDY PARTICIPANT DETAILS
  - Cell lines
  - Animals
  - Human PBMC and tissue microarray slide
- METHOD DETAILS
  - ELISA
  - Immunofluorescence
  - Co-immunoprecipitation
  - BLI affinity and epitope binning assay
  - Protein cross-linking and SDS-PAGE silver staining
  - Induction and detection of MDSCs
  - T cell proliferation assay
  - Transcriptome, morphology and cytokine analysis of immune cells
  - Establishment of stable cells
  - Immunoblotting and nuclear extraction
  - Ubiquitination assay of TRAF-6
  - Membrane and soluble IL-6R assay
  - Reporter cell assay
  - Flow cytometry assay
  - Epitope mapping
  - Antibody fab production
  - *In vivo* tumor models of phenotypes
  - *In vivo* tumor models of therapeutic effects
  - Flow cytometry analysis of *In vivo* tumor models
  - Immunohistochemistry
- QUANTIFICATION AND STATISTICAL ANALYSIS

SUPPLEMENTAL INFORMATION

Supplemental information can be found online at https://doi.org/10.1016/j.xcrm.2023.101374.

ACKNOWLEDGMENTS

This work was supported by the National Natural Science Foundation of China (nos. 82030104, 81874050, and 81572326), the Leading Talent of "Ten Thousand Plan" of China Basic Research Projects of Shanghai Science and Technology Innovation Action Plan (20JC1410700), the National Key R&D Program of China (2016YFC0906002), Tang Scholar (to J.X.), and Startup Research Funding of Fudan University.

Figure 6. Anti-Gal-8 monoclonal antibody that blocked Gal-8-LILRB4 interaction had a similar effect on tumor growth with anti-LILRB4 antibody

(A) Binding signals of Gal-8 antibody clones to human and cynomolgus antigens. The antibodies were developed by immunizing mice and identified by phage display technology.

(B) Results of epitope binning by the BLI system. The result was analyzed and visualized by Cytoscape 3.9.

(C) The blocking capacity of antibodies of different epitopes. The clone names for antibodies numbered 36 and 34 are A237 and A269, respectively.

(D) Competitive binding of LILRB4 and A269 to human Gal-8. In the BLI system, the probe was coated with A269 antibody following association with Gal-8 (step 1). Afterward, the association of LILRB4 was blocked by A269 but not A237, another Gal-8 antibody (step 2), indicating that clone A269 blocked the binding of Gal-8 and LILRB4.

(E and F) Binding kinetics of anti-Gal-8 antibody, clone A269 (E), and clone A237 (F) to human Gal-8 protein. A global fit of data was obtained from the association and dissociation phase with a 2-fold concentration series.

(G–J) Tumor growth curves and *ex vivo* tumor image for PBMC humanized A375 (G and H) and Hct116 (I and J) cell-line-derived tumor xenograft models. The drugs were given intraperitoneally once every 3 days as described.

(K and L) Tissue microarray analysis of Gal-8 expression in melanoma clinical samples. IHC staining of Gal-8 on 46 melanoma samples was scored and categorized.

(M and N) Treatment with the A269 antibody (anti-Gal-8) alone or in combination with atezolizumab (anti-PD-L1) in the MC38 *in vivo* transplant tumor model. MC38 cells overexpressing human Gal-8 were used to establish a subcutaneous graft tumor model. Drugs were given intraperitoneally once every 3 days. All of the statistical data in this figure were represented as mean ± SEM.

See also Figure S6.

AUTHOR CONTRIBUTIONS

Y.W., Y.S., S.D., J.L., J.Y., H.C., X.H., Y.Z., J.S., Y.W., and Y.Q. performed the experiments. Y.W., H.L., and J.X. wrote the manuscript. J.X. conceived and supervised the study.

DECLARATION OF INTERESTS

The authors have two patents related to this work, patent nos. CN 202311569533.7 and CN202111313462.5.

Received: April 2, 2023
Revised: September 16, 2023
Accepted: December 15, 2023
Published: January 16, 2024

REFERENCES

1. Sharma, P., and Allison, J.P. (2015). The future of immune checkpoint therapy. Science *348*, 56–61.
2. Topalian, S.L., Drake, C.G., and Pardoll, D.M. (2015). Immune checkpoint blockade: a common denominator approach to cancer therapy. Cancer Cell *27*, 450–461.
3. Veglia, F., Perego, M., and Gabrilovich, D. (2018). Myeloid-derived suppressor cells coming of age. Nat. Immunol. *19*, 108–119.
4. Fultang, L., Panetti, S., Ng, M., Collins, P., Graef, S., Rizkalla, N., Booth, S., Lenton, R., Noyvert, B., Shannon-Lowe, C., et al. (2019). MDSC targeting with Gemtuzumab ozogamicin restores T cell immunity and immunotherapy against cancers. EBioMedicine *47*, 235–246.
5. Loeuillard, E., Yang, J., Buckarma, E., Wang, J., Liu, Y., Conboy, C., Pavelko, K.D., Li, Y., O'Brien, D., Wang, C., et al. (2020). Targeting tumor-associated macrophages and granulocytic myeloid-derived suppressor cells augments PD-1 blockade in cholangiocarcinoma. J. Clin. Invest. *130*, 5380–5396.
6. Liu, F.T., and Rabinovich, G.A. (2005). Galectins as modulators of tumour progression. Nat. Rev. Cancer *5*, 29–41.
7. Quenum Zangbede, F.O., Chauhan, A., Sharma, J., and Mishra, B.B. (2018). Galectin-3 in M2 Macrophages Plays a Protective Role in Resolution of Neuropathology in Brain Parasitic Infection by Regulating Neutrophil Turnover. J. Neurosci. *38*, 6737–6750.
8. Yin, J., Li, L., Wang, C., and Zhang, Y. (2020). Increased Galectin-9 expression, a prognostic biomarker of aGVHD, regulates the immune response through the Galectin-9 induced MDSC pathway after allogeneic hematopoietic stem cell transplantation. Int. Immunopharmacol. *88*, 106929.
9. Zhang, C.X., Huang, D.J., Baloche, V., Zhang, L., Xu, J.X., Li, B.W., Zhao, X.R., He, J., Mai, H.Q., Chen, Q.Y., et al. (2020). Galectin-9 promotes a suppressive microenvironment in human cancer by enhancing STING degradation. Oncogenesis *9*, 65.
10. Liu, F.T., and Stowell, S.R. (2023). The role of galectins in immunity and infection. Nat. Rev. Immunol. *23*, 479–494.
11. Limagne, E., Richard, C., Thibaudin, M., Fumet, J.D., Truntzer, C., Lagrange, A., Favier, L., Coudert, B., and Ghiringhelli, F. (2019). Tim-3/galectin-9 pathway and mMDSC control primary and secondary resistances to PD-1 blockade in lung cancer patients. OncoImmunology *8*, e1564505.
12. Fujihara, S., Mori, H., Kobara, H., Rafiq, K., Niki, T., Hirashima, M., and Masaki, T. (2013). Galectin-9 in cancer therapy. Recent Pat. Endocr. Metab. Immune Drug Discov. *7*, 130–137.
13. Yang, R., Sun, L., Li, C.F., Wang, Y.H., Yao, J., Li, H., Yan, M., Chang, W.C., Hsu, J.M., Cha, J.H., et al. (2021). Galectin-9 interacts with PD-1 and TIM-3 to regulate T cell death and is a target for cancer immunotherapy. Nat. Commun. *12*, 832.
14. Elola, M.T., Ferragut, F., Cárdenas Delgado, V.M., Nugnes, L.G., Gentilini, L., Laderach, D., Troncoso, M.F., Compagno, D., Wolfenstein-Todel, C., and Rabinovich, G.A. (2014). Expression, localization and function of galectin-8, a tandem-repeat lectin, in human tumors. Histol. Histopathol. *29*, 1093–1105.
15. Beyer, S., Wehrmann, M., Meister, S., Kolben, T.M., Trillsch, F., Burges, A., Czogalla, B., Schmoeckel, E., Mahner, S., Jeschke, U., and Kolben, T. (2022). Galectin-8 and -9 as prognostic factors for cervical cancer. Arch. Gynecol. Obstet. *306*, 1211–1220.
16. Tribulatti, M.V., Carabelli, J., Prato, C.A., and Campetella, O. (2020). Galectin-8 in the onset of the immune response and inflammation. Glycobiology *30*, 134–142.
17. Su, Z.Z., Lin, J., Shen, R., Fisher, P.E., Goldstein, N.I., and Fisher, P.B. (1996). Surface-epitope masking and expression cloning identifies the human prostate carcinoma tumor antigen gene PCTA-1 a member of the galectin gene family. Proc. Natl. Acad. Sci. USA *93*, 7252–7257.
18. Ferragut, F., Cagnoni, A.J., Colombo, L.L., Sánchez Terrero, C., Wolfenstein-Todel, C., Troncoso, M.F., Vanzulli, S.I., Rabinovich, G.A., Mariño, K.V., and Elola, M.T. (2019). Dual knockdown of Galectin-8 and its glycosylated ligand, the activated leukocyte cell adhesion molecule (ALCAM/CD166), synergistically delays in vivo breast cancer growth. Biochim. Biophys. Acta. Mol. Cell Res. *1866*, 1338–1352.
19. Deng, M., Gui, X., Kim, J., Xie, L., Chen, W., Li, Z., He, L., Chen, Y., Chen, H., Luo, W., et al. (2018). LILRB4 signalling in leukaemia cells mediates T cell suppression and tumour infiltration. Nature *562*, 605–609.
20. de Goeje, P.L., Bezemer, K., Heuvers, M.E., Dingemans, A.M.C., Groen, H.J., Smit, E.F., Hoogsteden, H.C., Hendriks, R.W., Aerts, J.G., and Hegmans, J.P. (2015). Immunoglobulin-like transcript 3 is expressed by myeloid-derived suppressor cells and correlates with survival in patients with non-small cell lung cancer. OncoImmunology *4*, e1014242.
21. Singh, L., Muise, E.S., Bhattacharya, A., Grein, J., Javaid, S., Stivers, P., Zhang, J., Qu, Y., Joyce-Shaikh, B., Loboda, A., et al. (2021). ILT3 (LILRB4) Promotes the Immunosuppressive Function of Tumor-Educated Human Monocytic Myeloid-Derived Suppressor Cells. Mol. Cancer Res. *19*, 702–716.
22. Liu, J., Wu, Q., Shi, J., Guo, W., Jiang, X., Zhou, B., and Ren, C. (2020). LILRB4, from the immune system to the disease target. Am. J. Transl. Res. *12*, 3149–3166.
23. Su, M.T., Kumata, S., Endo, S., Okada, Y., and Takai, T. (2022). LILRB4 promotes tumor metastasis by regulating MDSCs and inhibiting miR-1 family miRNAs. OncoImmunology *11*, 2060907.
24. Sharma, N., Atolagbe, O.T., Ge, Z., and Allison, J.P. (2021). LILRB4 suppresses immunity in solid tumors and is a potential target for immunotherapy. J. Exp. Med. *218*, e20201811.
25. Brandish, P.E., Palmieri, A., Ayanoglu, G., Baker, J., Bueno, R., Byford, A., Caniga, M., Chappell, C., Cherwinski, H., Cua, D.J., et al. (2021). Antibodies to ILT3 abrogate myeloid immunosuppression and enable tumor killing. Preprint at bioRxiv.
26. Naing, A., Wang, J.S., Sharma, M.R., Sommerhalder, D., Gandhi, L., Oh, D.-Y., Jiang, Y., Michalski, J., Lee, J., Zhou, K., et al. (2022). First-in-human Study of NGM707, an ILT2/ILT4 Dual Antagonist Antibody in Advanced or Metastatic Solid Tumors: Preliminary Monotherapy Dose Escalation Data (Elsevier Inc.).
27. Macdonald-Obermann, J.L., and Pike, L.J. (2014). Different epidermal growth factor (EGF) receptor ligands show distinct kinetics and biased or partial agonism for homodimer and heterodimer formation. J. Biol. Chem. *289*, 26178–26188.
28. Zizzari, I.G., Napoletano, C., Battisti, F., Rahimi, H., Caponnetto, S., Pierelli, L., Nuti, M., and Rughetti, A. (2015). MGL Receptor and Immunity: When the Ligand Can Make the Difference. J. Immunol. Res. *2015*, 450695.
29. Fuselier, C., Dumoulin, A., Pare, A., Nehme, R., Ajarrag, S., Granger Joly de Boissel, P., Chatenet, D., Doucet, N., and St-Pierre, Y. (2023). Placental Galectins in Cancer: Why We Should Pay More Attention. Cells *12*, 437.
30. Moreno, P., Fexova, S., George, N., Manning, J.R., Miao, Z., Mohammed, S., Muñoz-Pomer, A., Fullgrabe, A., Bi, Y., Bush, N., et al. (2022).

Expression Atlas update: gene and protein expression in multiple species. Nucleic Acids Res. *50*, D129–D140.

31. Fu, J., Li, K., Zhang, W., Wan, C., Zhang, J., Jiang, P., and Liu, X.S. (2020). Large-scale public data reuse to model immunotherapy response and resistance. Genome Med. *12*, 21.
32. Li, T., Fu, J., Zeng, Z., Cohen, D., Li, J., Chen, Q., Li, B., and Liu, X.S. (2020). TIMER2.0 for analysis of tumor-infiltrating immune cells. Nucleic Acids Res. *48*, W509–W514.
33. Maute, R.L., Gordon, S.R., Mayer, A.T., McCracken, M.N., Natarajan, A., Ring, N.G., Kimura, R., Tsai, J.M., Manglik, A., Kruse, A.C., et al. (2015). Engineering high-affinity PD-1 variants for optimized immunotherapy and immuno-PET imaging. Proc. Natl. Acad. Sci. USA *112*, E6506–E6514.
34. Chen, H.M., van der Touw, W., Wang, Y.S., Kang, K., Mai, S., Zhang, J., Alsina-Beauchamp, D., Duty, J.A., Mungamuri, S.K., Zhang, B., et al. (2018). Blocking immunoinhibitory receptor LILRB2 reprograms tumor-associated myeloid cells and promotes antitumor immunity. J. Clin. Invest. *128*, 5647–5662.
35. Chanput, W., Mes, J.J., and Wichers, H.J. (2014). THP-1 cell line: an in vitro cell model for immune modulation approach. Int. Immunopharmacol. *23*, 37–45.
36. Fernandes, R.A., Su, L., Nishiga, Y., Ren, J., Bhuiyan, A.M., Cheng, N., Kuo, C.J., Picton, L.K., Ohtsuki, S., Majzner, R.G., et al. (2020). Immune receptor inhibition through enforced phosphatase recruitment. Nature *586*, 779–784.
37. Lu, H.K., Rentero, C., Raftery, M.J., Borges, L., Bryant, K., and Tedla, N. (2009). Leukocyte Ig-like receptor B4 (LILRB4) is a potent inhibitor of FcgammaRI-mediated monocyte activation via dephosphorylation of multiple kinases. J. Biol. Chem. *284*, 34839–34848.
38. Xu, D., and Qu, C.K. (2008). Protein tyrosine phosphatases in the JAK/STAT pathway. Front. Biosci. *13*, 4925–4932.
39. Bu, L.L., Yu, G.T., Deng, W.W., Mao, L., Liu, J.F., Ma, S.R., Fan, T.F., Hall, B., Kulkarni, A.B., Zhang, W.F., and Sun, Z.J. (2016). Targeting STAT3 signaling reduces immunosuppressive myeloid cells in head and neck squamous cell carcinoma. OncoImmunology *5*, e1130206.
40. Li, J., Gao, A., Zhang, F., Wang, S., Wang, J., Wang, J., Han, S., Yang, Z., Chen, X., Fang, Y., et al. (2021). ILT3 promotes tumor cell motility and angiogenesis in non-small cell lung cancer. Cancer Lett. *501*, 263–276.
41. Li, Z., Deng, M., Huang, F., Jin, C., Sun, S., Chen, H., Liu, X., He, L., Sadek, A.H., and Zhang, C.C. (2020). LILRB4 ITIMs mediate the T cell suppression and infiltration of acute myeloid leukemia cells. Cell. Mol. Immunol. *17*, 272–282.
42. Hao, Z., Li, R., Wang, Y., Li, S., Hong, Z., and Han, Z. (2021). Landscape of Myeloid-derived Suppressor Cell in Tumor Immunotherapy. Biomark. Res. *9*, 77.
43. Zhao, F., Hoechst, B., Duffy, A., Gamrekelashvili, J., Fioravanti, S., Manns, M.P., Greten, T.F., and Korangy, F. (2012). S100A9 a new marker for monocytic human myeloid-derived suppressor cells. Immunology *136*, 176–183.
44. McFarland, B.C., Gray, G.K., Nozell, S.E., Hong, S.W., and Benveniste, E.N. (2013). Activation of the NF-kappaB pathway by the STAT3 inhibitor JSI-124 in human glioblastoma cells. Mol. Cancer Res. *11*, 494–505.
45. Lu, Y., Jiang, Z., Dai, H., Miao, R., Shu, J., Gu, H., Liu, X., Huang, Z., Yang, G., Chen, A.F., et al. (2018). Hepatic leukocyte immunoglobulin-like receptor B4 (LILRB4) attenuates nonalcoholic fatty liver disease via SHP1-TRAF6 pathway. Hepatology *67*, 1303–1319.
46. Fang, J., Muto, T., Kleppe, M., Bolanos, L.C., Hueneman, K.M., Walker, C.S., Sampson, L., Wellendorf, A.M., Chetal, K., Choi, K., et al. (2018). TRAF6 Mediates Basal Activation of NF-kappaB Necessary for Hematopoietic Stem Cell Homeostasis. Cell Rep. *22*, 1250–1262.
47. Jakus, P.B., Kalman, N., Antus, C., Radnai, B., Tucsek, Z., Gallyas, F., Jr., Sumegi, B., and Veres, B. (2013). TRAF6 is functional in inhibition of TLR4-mediated NF-kappaB activation by resveratrol. J. Nutr. Biochem. *24*, 819–823.
48. Wawro, K., Wawro, M., Strzelecka, M., Czarnek, M., and Bereta, J. (2019). The role of NF-kappaB and Elk-1 in the regulation of mouse ADAM17 expression. Biol. Open *8*, bio039420.
49. Scheller, J., Chalaris, A., Garbers, C., and Rose-John, S. (2011). ADAM17: a molecular switch to control inflammation and tissue regeneration. Trends Immunol. *32*, 380–387.
50. Lambrecht, B.N., Vanderkerken, M., and Hammad, H. (2018). The emerging role of ADAM metalloproteinases in immunity. Nat. Rev. Immunol. *18*, 745–758.
51. Orme, J.J., Jazieh, K.A., Xie, T., Harrington, S., Liu, X., Ball, M., Madden, B., Charlesworth, M.C., Azam, T.U., Lucien, F., et al. (2020). ADAM10 and ADAM17 cleave PD-L1 to mediate PD-(L)1 inhibitor resistance. OncoImmunology *9*, 1744980.
52. Zhu, Z., Zhang, H., Zhang, X., He, S., Dong, W., Wang, X., Chen, Y., Liu, X., and Guo, C. (2020). Lipopolysaccharide Downregulates CD163 Expression to Inhibit PRRSV Infection via TLR4-NF-kappaB Pathway. Front. Microbiol. *11*, 501.
53. Pal, S., Nandi, M., Dey, D., Chakraborty, B.C., Shil, A., Ghosh, S., Banerjee, S., Santra, A., Ahammed, S.K.M., Chowdhury, A., and Datta, S. (2019). Myeloid-derived suppressor cells induce regulatory T cells in chronically HBV infected patients with high levels of hepatitis B surface antigen and persist after antiviral therapy. Aliment. Pharmacol. Ther. *49*, 1346–1359.
54. Yaddanapudi, K., Rendon, B.E., Lamont, G., Kim, E.J., Al Rayyan, N., Richie, J., Albeituni, S., Waigel, S., Wise, A., and Mitchell, R.A. (2016). MIF Is Necessary for Late-Stage Melanoma Patient MDSC Immune Suppression and Differentiation. Cancer Immunol. Res. *4*, 101–112.
55. Juneja, V.R., McGuire, K.A., Manguso, R.T., LaFleur, M.W., Collins, N., Haining, W.N., Freeman, G.J., and Sharpe, A.H. (2017). PD-L1 on tumor cells is sufficient for immune evasion in immunogenic tumors and inhibits CD8 T cell cytotoxicity. J. Exp. Med. *214*, 895–904.
56. Gabrilovich, D.I., Ostrand-Rosenberg, S., and Bronte, V. (2012). Coordinated regulation of myeloid cells by tumours. Nat. Rev. Immunol. *12*, 253–268.
57. Lalle, G., Twardowski, J., and Grinberg-Bleyer, Y. (2021). NF-kappaB in Cancer Immunity: Friend or Foe? Cells *10*, 355.
58. Zhu, F., Yue, W., and Wang, Y. (2014). The nuclear factor kappa B (NF-kappaB) activation is required for phagocytosis of staphylococcus aureus by RAW 264.7 cells. Exp. Cell Res. *327*, 256–263.
59. Fan, Y., Mao, R., and Yang, J. (2013). NF-kappaB and STAT3 signaling pathways collaboratively link inflammation to cancer. Protein Cell *4*, 176–185.
60. Karin, N. (2020). The Development and Homing of Myeloid-Derived Suppressor Cells: From a Two-Stage Model to a Multistep Narrative. Front. Immunol. *11*, 557586.
61. Korotkevich, G., Sukhov, V., Budin, N., Shpak, B., Artyomov, M.N., and Sergushichev, A. (2019). Fast gene set enrichment analysis. Preprint at bioRxiv.
62. Kevin, B., Rana, S., and Lewis, M. (2022). EnhancedVolcano: Publication-Ready Volcano Plots with Enhanced Colouring and Labeling.
63. H. Wickham, ed. (2016). ggplot2: Elegant Graphics for Data Analysis (Springer-Verlag).
64. Slowikowski, K. (2023). Ggrepel: Automatically Position Non-overlapping Text Labels with (ggplot2).
65. Pagès, H., Carlson, M., and Li, S.F.a.N. (2022). AnnotationDbi: Manipulation of SQLite-Based Annotations in Bioconductor.
66. Wu, T., Hu, E., Xu, S., Chen, M., Guo, P., Dai, Z., Feng, T., Zhou, L., Tang, W., Zhan, L., et al. (2021). clusterProfiler 4.0: A universal enrichment tool for interpreting omics data. Innovation *2*, 100141.

STAR★METHODS

KEY RESOURCES TABLE

REAGENT or RESOURCE	SOURCE	IDENTIFIER
Antibodies		
Mouse monoclonal anti-DYKDDDDK Tag (Clone 9A3A1F2)	Cell Signaling Technology (CST)	Cat#8146S; RRID: AB_10950495
Rabbit monoclonal anti-DYKDDDDK Tag (Clone D6W5B)	CST	Cat#14793S; RRID: AB_2572291
Mouse monoclonal anti-HA Tag (Clone F-7)	Santa Cruz Biotechnology	Cat#sc-7392; RRID: AB_627809
Rabbit monoclonal anti-HA Tag (Clone C29F4A12)	CST	Cat#3724S; RRID: AB_1549585
Goat anti-Mouse IgG, Alexa Fluor™ 488	Invitrogen	Cat#A-21202; RRID: AB_2534069
Goat anti-Human IgG, Alexa Fluor™ 488	Invitrogen	Cat#A-11013; RRID: AB_2534080
Donkey anti-Rabbit IgG, Alexa Fluor™ 594	Invitrogen	Cat#A-21207; RRID: AB_141637
Goat anti-Human IgG, Alexa Fluor™ 647	Invitrogen	Cat#A-21445; RRID: AB_2535862
Mouse IgG Isotype	Beyotime	Cat#A7028; RRID: AB_2909433
Rabbit IgG Isotype	Beyotime	Cat#A7016; RRID: AB_2905533
Goat Anti-Human IgG, HRP	Jackson ImmunoResearch	Cat#109-035-003; RRID: AB_2337577
Goat anti-Mouse IgG, HRP	Shanghai Aksomics	Cat#KC-MM-035; RRID: AB_2665472
Goat anti-Rabbit IgG, HRP	Shanghai Aksomics	Cat#KC-RB-035; RRID: AB_2631281
Rat monoclonal anti-CD11b, APC (CloneM1/70)	Invitrogen	CAT#17-0112-82; RRID: AB_2535403
Mouse monoclonal anti-human CD33, PE (Clone WM53)	Biolegend	CAT#303404; RRID: AB_314348
Mouse monoclonal anti-human HLA-DR, APC/Cyanine7 (Clone L243)	Biolegend	Cat#307618; RRID: AB_493586
Rat monoclonal anti-CD3, APC (Clone 17A2)	Biolegend	Cat#100236; RRID: AB_2561456
Rabbit polyclonal anti-phospho-SHIP-1 (Tyr1020)	CST	Cat#3941T; RRID: AB_2296062
Mouse monoclonal anti-SHIP-1 (Clone P1C1)	Santa Cruz Biotechnology	Cat#sc-8425; RRID: AB_628250
Recombinant Rabbit anti-phospho-SHP-1 (Clone D11G5D2)	CST	Cat#8849T; RRID: AB_11141050
Mouse monoclonal anti-SHP-1 (Clone D-11)	Santa Cruz Biotechnology	Cat#sc-7289; RRID: AB_628251
Rabbit polyclonal anti-phospho-SHP-2 (Tyr542)	CST	Cat#3751T; RRID: AB_330825
Mouse monoclonal anti-SHP-2 (Clone B-1)	Santa Cruz Biotechnology	Cat#sc-7384; RRID: AB_628252
Mouse monoclonal anti-STAT3 (Clone 124H6D3)	CST	Cat#9139S; RRID: AB_331757
Recombinant Rabbit anti-phospho-STAT3 (Tyr705) (Clone D3A7)	CST	Cat#9145S; RRID: AB_2491009
Rabbit polyclonal anti-phospho-STAT3(Ser727)	CST	Cat#9134T; RRID: AB_331589
Recombinant Rabbit anti-phospho-NF-κB p65 (Clone 93H1)	CST	Cat#3033S; RRID: AB_331284
Recombinant Rabbit anti-NF-κB p65 (Clone D14E12B3)	CST	Cat#8242S; RRID: AB_10859369
Recombinant Rabbit anti-phospho-AKT (Clone D9)	CST	Cat#4060S; RRID: AB_2315049
Recombinant Rabbit anti-Akt (Clone C67E7B4)	CST	Cat#4691S; RRID: AB_915783
Mouse monoclonal anti-*p*-ERK 1/2 (clone 12D4)	Santa Cruz Biotechnology	Cat#sc-81492; RRID: AB_1125801
Mouse monocalonal anti-ERK 1/2 (Clone C-9)	Santa Cruz Biotechnology	Car#sc-514302; RRID: AB_2571739
Rabbit polyclonal anti-LILRB4	GeneTex	Cat#GTX33296; RRID: AB_2887707
Rabbit polyclonal anti-SCOS3	Abcam	Cat#ab16030; RRID: AB_443287

(*Continued on next page*)

Continued

REAGENT or RESOURCE	SOURCE	IDENTIFIER
Mouse monoclonal anti-GAPDH, HRP	Shanghai Aksomics	Cat#KC-5G5; RRID: AB_2631280
Mouse monoclonal anti-β-Actin, HRP	Shanghai Aksomics	Cat#KC-5A08; RRID: AB_2847811
Rabbit monoclonal anti-Lamin B1 (Clone D4Q4Z)	CST	Cat#12586T; RRID: AB_2650517
Rabbit polyclonal anti-α-Tubulin	Affinity Biosciences	Cat#AF7010; RRID: AB_2839418
Mouse anti-human CD3 (Clone OKT3)	Invitrogen	Cat#14-0037-82; RRID: AB_467057
Mouse anti-human CD28 (Clone CD28.2)	Invitrogen	Cat#16-0289-81; RRID: AB_468926
Rabbit polyclonal anti-S100A8	ProteinTech	Cat#15792-1-AP; RRID: 10666315
Rabbit polyclonal anti-S100A9	ProteinTech	Cat#26992-1-AP; RRID: AB_2880716
Rabbit monoclonal anti-K63-linkage specific polyubiquitin (Clone D7A11)	CST	Cat#5621T; RRID: AB_10827985
Rabbit monoclonal anti-TRAF6 (Clone D21G3)	CST	Cat#8028T; RRID: AB_10858223
Rabbit monoclonal anti-PD-L1 (Clone E1L3N)	CST	Cat#13684S; RRID: AB_2687655
Mouse monoclonal anti-human-CD163 (Clone GHI/61)	Biolegend	Cat#333602; RRID: AB_1088991
Rabbit polyclonal anti-ADAM17	Abcam	Cat#ab2051; RRID: AB_302796
Donkey Anti-rabbit IgG, PE	Biolegend	Cat#406421; RRID: AB_2563484
Mouse monoclonal anti-IL-6R, PE/Cyanine7 (Clone UV4)	Biolegend	Cat#352809; RRID: AB_2562716
Mouse IgG1 Isotype, PE/Cyanine7	Biolegend	Cat#400125; RRID: AB_2861433
Rat monoclonal anti-Ly-6C, FITC (Clone HK1.4)	Biolegend	Cat#128006; RRID: AB_1186135
Rat monoclonal anti-Ly-6G, PerCP/Cyanine5.5 (Clone 1A8)	Biolegend	Cat#127616; RRID: AB_1877272
Rat anti-mouse CD16/32	Biolegend	Cat#101302; RRID: AB_312801
Recombinant rabbit anti-CD8 (Clone EPR21769)	Abcam	Cat#ab217344; RRID: AB_2890649
Recombinant rabbit Anti-FOXP3 (Clone D6O8R)	CST	Cat#12653S; RRID: AB_2797979
Rabbit monoclonal anti-Galectin-8 (Clone EPR4857)	Abcam	Cat#ab109519; RRID: AB_10861755
Rabbit polyclonal antibody to LGALS8	Biorbyt	Cat#orb216142; RRID: AB_3076638
Biological samples		
Cryopreserved human PBMC derived from healthy patients	Shanghai Saily Biotechnology	Cat#PB010/PB025
Tissue microarray of human melanoma	Xi'an TaibsBio	Cat#MME1004i
Chemicals, peptides, and recombinant proteins		
ELISA coating buffer	Beijing Solarbio	Cat#C1055
PBS	Dalian Meilunbio	Cat#MA0015
TBS	Sangon	Cat#B548105
Tween 20	Beijing Solarbio	Cat#T8220
TMB Single-Component Substrate solution	Beijing Solarbio	Cat#PR1200
Fetal Bovine Serum (FBS)	Gibco™	Cat#10099158
DMEM, High Glucose	Dalian Meilunbio	Cat#MA0212
RPMI 1640	Dalian Meilunbio	Cat#MA0215
Paraformaldehyde, 4%	Beijing Solarbio	Cat#P1110
Triton X-100	Sigma-Aldrich	Cat#93443
DAPI Fluoromount-G®	SounthernBiotech	Cat#0100-20
Pierce™ IP lysis buffer	Thermo Scientific	Cat#87787
Pierce™ Protein G Agarose	Thermo Scientific	Cat#20398
RIPA Lysis Buffer	Thermo Scientific	Cat#89901
Bovine Serum Albumin (BSA)	VWR Life Science	Cat#97061-420
Protein-free rapid blocking buffer	Shanghai Epizyme	Cat#PS108
Recombinant human LILRB4 protein (ECD, His Tag)	Sino Biological	Cat#16742-H08H
Recombinant human LILRB4 protein (ECD, hFc Tag)	Sino Biological	Cat#16742-H02H

(*Continued on next page*)

Continued

REAGENT or RESOURCE	SOURCE	IDENTIFIER
Recombinant human Galectin 8/LGALS8 protein	Sino Biological	Cat#10301-HNAE
Recombinant human CD3ε protein (ECD, hFc Tag)	Sino Biological	Cat#10977-H02H
Recombinant human CTLA-4 protein (ECD, hFc Tag)	Acro Biosystems	Cat#CT4-H5255
Recombinant human CD28 protein (ECD, hFc Tag)	Acro Biosystems	Cat#CD8-H525a
Recombinant human CD96 protein (ECD, hFc Tag)	Acro Biosystems	Cat#TAE-H5252
Recombinant human LAG-3 protein (ECD, hFc Tag)	Acro Biosystems	Cat#LA3-H5255
Recombinant human TIM-3 protein (ECD, hFc Tag)	Acro Biosystems	Cat#TM3-H5258
Recombinant human CD40 protein (ECD, hFc Tag)	Acro Biosystems	Cat#CD0-5253
Recombinant human ICOS protein (ECD, hFc Tag)	Acro Biosystems	Cat#ICS-H5258
Recombinant human OX40 protein (ECD, hFc Tag)	Acro Biosystems	Cat#OX0-H5255
Recombinant human TIGIT protein (ECD, hFc Tag)	Acro Biosystems	Cat#TIT-H525
Recombinant human CD27 protein (ECD, hFc Tag)	Acro Biosystems	Cat#CD7-H5254
Recombinant human LY86 protein (ECD, hFc Tag)	Sino Biological	Cat#10242-H02H
Recombinant human PD-1 protein (ECD, hFc Tag)	Sino Biological	Cat#10377-H02
Recombinant human CD8b protein (ECD, hFc Tag)	Sino Biological	Cat#11031-HCCH
Penicillin-Streptomycin	Dalian Meilunbio	Cat#MA0110
0.25%Trypsin-EDTA with PhenolRed	Dalian Meilunbio	Cat#PWL060
Super ECL Detection Reagent	Shanghai Yeasen	Cat#36208ES60
Human TruStain FcX™	BioLegend	Cat#422301
Dimethyl sulfoxide (DMSO)	Sigma-Aldrich	Cat#D8418
Glycine, Molecular Biology Grade, CAS#56-40-6	Sangon	Cat#A610235
SDS, Molecular Biology Grade, CAS#151-21-3	Sangon	Cat#A600485
Tris, Molecular Biology Grade, CAS#77-86-1	Sangon	Cat#A600194
Glutaric dialdehyde, Grade II, 25% in H2O, CAS#111-30-8	Sinopharm	Cat#30092436
0.4% trypan blue stain	Invitrogen	Cat#T10282
TRIzol Reagent	Invitrogen	Cat#15596026
FuGENE® HD Transfection Reagent	Promega	Cat#E2312
Human Apolipoprotein E Protein, Tag Free	Acro Biosystems	APE-H5216
Recombinant Human Granulocyte-Macrophage Colony Stimulating Factor	Sangon	Cat#C610017
5X SDS-PAGE protein loading buffer	Beyotime	Cat#0015
Pierce™ Lane Marker Non-ruducing Sample Buffers	Thermo Scientific	Cat#39001
Zombie Aqua™ Fixable Viability Kit	Biolegend	Cat#423102
eBioscience™ Flow Cytometry Staining Buffer	Invitrogen	Cat#00-4222-26
eBioscience™ intracellular fixation and permeabilization buffer	Invitrogen	Cat#88-8823-88
Protease and Phosphatase Inhibitor and PMSF (100X)	Shanghai Aksomics	Cat#KC-440
puromycin	InvivoGen	Cat. Code: ant-pr
Normocin™	InvivoGen	Cat. Code: ant-nr
Zeocin®	InvivoGen	Cat. Code: ant-zn
Blasticidin	InvivoGen	Cat. Code: ant-bl
Pam3CSK4	InvivoGen	Cat. Code: tlrl-pms
Geneticin™ Selective Antibiotic (G418 Sulfate)	Gibco	Cat#10131027
dsDNase	QIAGEN	Cat#EN33-050
Recombinant Human IL-2	PeproTech	Cat#200-02
Quanti-blueTM Alkaline phosphatase detection medium	InvivoGen	Cat. Code: rep-qbs
Recombinant Mouse LILRB4 protein, Fc tag	Acro Biosystems	Cat#CDK-M5250
Percoll density gradient media	Cytiva	Cat#17089101
DNAse I, CAS: 9003-98-9	Sigma-Aldrich	Cat#D4527
Collagenase, CAS: 9001-12-1	Sigma-Aldrich	Cat#C2674

(*Continued on next page*)

Continued

REAGENT or RESOURCE	SOURCE	IDENTIFIER
Ack Lysis buffer	Beyotime	Cat#C3702
EDTA-2K solution (10x)	Beijing Solarbio	Cat#G0280
Citrate Antigen Retrieval Solution	Beyotime	Cat#P0081
Supervision™ Universal HRP-conjugated anti-mouse/rabbit antibody	Shanghai Changdao	Cat#D3004
Neutral balsam	Biosharp	Cat#BL704A
Peptides as shown in Tables 1 and 2	Nanjing GeneScript	Design ID: C5202GG120, C5149GG290
Streptavidin-HRP	Nanjing GeneScript	Cat#M00091
STAT3 inhibitor	SelleckChem	Cat#S6570
Oligonucleotides		
Lentivirus: LILRB4 shRNA, Vector: hU6-MCS-Ubiquitin-EGFP-IRES-puromycin	Shanghai GeneChem	Design ID: GIEL0223634
Lentivirus: negative control, Vector: hU6-MCS-Ubiquitin-EGFP-IRES-puromycin	Shanghai GeneChem	N/A
Recombinant DNA		
Plasmid: pcDNA3.1-LGALS8 C-terminal FLAG-tagged	Shanghai Generay	N/A
Plasmid: pcDNA3.1-LILRB4 C-terminal HA-tagged	Shanghai Generay	N/A
Plasmid: pcDNA3.1-IgG1Fc-LGALS8	Shanghai Generay	N/A
Critical commercial assays		
Rapid Silver-staining Kit	Beyotime	Cat#P0017S
Coomassie Blue Staining Kit	Beyotime	Cat#P0017A
Omni-Easy™One-Step PAGE Gel Fast Preparation Kit	Shanghai Epizyme	Cat#PG212
Human IL-10 Elisa Kit	Beijing Solarbio	Cat#SEKH-0018
Enhanced BCA Protein Assay Kit)	Beyotime	Cat#P0010
CellTrace™ CFSE Cell Proliferation Kit	Invitrogen	Cat#C34554
EasySep™ Human CD14 Positive Selection Kit II	StemCell	Cat#100-0694
NE-PER™ Nuclear and Cytoplasmic Extraction Kit	Thermo Scientific	Cat#78833
Human Soluble Interleukin 6 Receptor ELISA Kit	Wuhan Elabscience	Cat#E-EL-H2518
DAB Horseradish Peroxidase Color Development Kit	Beyotime	Cat#P0203
Biotin labeling kit	Wuhan Elabscience	Cat#E-LK-B002
Pierce™ Fab preparation kit	Thermo Scientific	Cat#44985
Hematoxylin and Eosin Staining Kit	Beyotime	Cat#C0105S
Deposited data		
RNA expression of LGALS8 in Single cell types	The Human Protein Atlas: v23.0.proteinatlas.org	https://www.proteinatlas.org/ENSG00000116977-LGALS8/single+cell+type
$CD14^+$ cell transcriptome data	This study	GEO: GSE227527
PBMC transcriptome data	This study	GEO: GSE243947
Experimental models: Cell lines		
HEK293	National Collection of Authenticated Cell Culture	Cat#SCSP-5209
B16	National Collection of Authenticated Cell Culture	Cat#SCSP-5096
MC38	Kerafast	Cat#ENH204-FP
THP-1	Shanghai Huzhen	Cat#HZ51395CE
MV411	Shanghai Huzhen	Cat#HZ51263CE
HCT116	ATCC	Cat#CCL-247
A375	ATCC	Cat#CRL-1619
THP-1 reporter cells	InvivoGen	Cat. Code: thpd-nfis

(*Continued on next page*)

Continued

REAGENT or RESOURCE	SOURCE	IDENTIFIER
Experimental models: Organisms/strains		
Mouse: C57BL/6Smoc-Lilrb4a^{em1Smoc}	Shanghai Model Organisms Center (SMOC)	Cat#NM-KO-200727
Mouse: C57BL/6Smoc-Lilrb4a$^{em1(hLILRB4)Smoc}$	SMOC	Cat#NM-HU-210024
Mouse: C57BL/6Smoc	SMOC	Cat#SM-001
Mouse: NCG (NOD/ShiLtJGpt-Prkdc^{em26Cd52} Il2rg^{em26Cd22}/Gpt	Gempharmatech	Cat#T001475
Software and algorithms		
the Tumor Immune Dysfunction and Exclusion (TIDE)	Dana Farber Cancer Institute & Harvard University	http://tide.dfci.harvard.edu/
TIMER v2.0	Dana Farber Cancer Institute-X Shirley Liu Lab[32]	http://timer.cistrome.org/
Flowjo (v10)	TreeStar	https://www.flowjo.com
R (Version 4.2.1)	R Core	https://www.r-project.org/
R code	Zenodo	https://doi.org/10.5281/zenodo.10371383 https://zenodo.org/doi/10.5281/zenodo.10371382
fgsea R package	Sergushichev et al.[61]	https://bioconductor.org/packages/release/bioc/html/fgsea.html
EnhancedVolcano R package	Kevin Blighe et al.[62]	https://www.bioconductor.org/packages/release/bioc/html/EnhancedVolcano.html
ggplot2 R package	H. Wickham[63]	https://bioconductor.org/help/search/index.html?q=ggplot2/
ggrepel R package	Kamil Slowikowski[64]	https://bioconductor.org/help/search/index.html?q=ggrepel/
AnnotationDbi R package	Hervé Pagès et al.[65]	https://bioconductor.org/packages/release/bioc/html/AnnotationDbi.html
clusterProfiler R package	T. Wu[66]	https://bioconductor.org/packages/release/bioc/html/clusterProfiler.html
MSigDB	GSEA	https://www.gsea-msigdb.org/gsea/msigdb/index.jsp.
ImageJ (V.2.0.0-rc-69/1.52p)	NIH	https://imagej.nih.gov/ij/
Graphpad Prism 9 (Version 9.5.0)	Dotmatics	https://www.graphpad.com/
Cytoscape 3.9.1	National Institute of General Medical Sciences of the NIH	https://cytoscape.org

RESOURCE AVAILABILITY

Lead contact

Further information and requests for resources and reagents should be directed to and will be fulfilled by the lead contact, Jie Xu (jie_xu@fudan.edu.cn).

Materials availability

All unique/stable reagents generated in this study are available from the corresponding author Jie Xu (jie_xu@fudan.edu.cn) with a completed Materials Transfer Agreement.

Data and code availability

- RNA-seq data have been deposited at GEO and are publicly available as of the date of publication. Accession numbers are listed in the Key resources table. Original western blot images and microscopy data reported in this paper will be shared by the lead contact upon request.
- All original code has been deposited at Zenodo and is publicly available as of the date of publication. DOIs are listed in the Key resources table.

- Any additional information required to reanalyze the data reported in this work paper is available from the lead contact upon request.

EXPERIMENTAL MODEL AND STUDY PARTICIPANT DETAILS

Cell lines

HEK293 cells (SCSP-5209, NCACC), MC38 cells (ENH204-FP, Kerafast), and A375 cells (CRL-1619, ATCC) were cultured in DMEM supplemented with 10% FBS. THP-1 cells (HZ51395CE, Huzhen) and MV411 cells (HZ51263CE, Huzhen) were cultured in RPMI1640 supplemented with 10% heat-inactivated FBS. B16 cells (SCSP-5096, NCACC) and HCT116 cells (CCL-247, ATCC) were cultured in RPMI1640 supplemented with 10% FBS. THP-1 reporter cells (thpd-nfis, InvivoGen) were cultured in RPMI1640 supplemented with 10% heat-inactivated FBS, Normocin, Zeocin and Blasticidin, per manufacturer's instructions. All cell lines were maintained at 37°C in a humidified incubator at 5% CO_2.

Animals

4–6 weeks old female lilrb4a-KO C57BL6 mice (NM-KO-200727, SMOC), hLILRB4 C57BL6 mice (NM-HU-210024, SMOC) or HCG mice (T001475, Gempharmatech) were maintained under standardized conditions with a 12 h/day light cycle and controlled temperature (20°C–22°C) and humidity (40–60%). All mice studies were performed according to Regulations for Care and Use of Laboratory Animals at Fudan University and were approved by Fudan University Institutional Animal Care and Use Committee (IACUC).

Human PBMC and tissue microarray slide

Human PBMCs were purchased from Shanghai Saily Biological Technology and cultured in RPMI1640 supplemented with 10% heat-inactivated FBS. Tissue microarray slide was purchased from Xi'an Taibs Biotechnology (MME1004i, TaibsBio). Shanghai Saily Biological Technology and Xi'an Taibs Biotechnology represents and warrants that it has obtained ownership rights with respect to products and that such products were provided to Shanghai Saily Biological Technology and Xi'an Taibs Biotechnology with every donor's informed consent and in compliance with all applicable laws and regulations.

METHOD DETAILS

ELISA

The high-affinity 96-well ELISA plate (42592, Costar) were coated with recombinant Gal-8 (10301-HNAE; Sino Biological) protein and incubated at 4°C overnight. The plate was then washed with PBST (PBS, 0.05% Tween 20) (MA0015, Meilunbio) (T8220, Solarbio) and blocked with 3% BSA (97061-420, VWR) at 37°C for 90 min. After repeated washing, hFc-tagged recombinant proteins, including CD3ε (10977-H02H; Sino Biological), CTLA-4 (CT4-H5255; Acro Biosystems), CD28 (CD8-H525a; Acro Biosystems), CD96 (TAE-H5252; Acro Biosystems), LAG-3 (LA3-H5255; Acro Biosystems), TIM-3 (TM3-H5258; Acro Biosystems), CD40 (CD0-5253; Acro Biosystems), ICOS (ICS-H5258; Acro biosystems), OX40 (OX0-H5255; Acro Biosystems), TIGHT (TIT-H5254; Acro Biosystems), LY86 (10242-H02H; Sino Biological), LILRB4 (16742-H02H; Sino Biological), CD27 (CD7-H5254; Acro biosystems), PD-1 (10377-H02H; Sino Biological), and CD8b (11031-HCCH; Sino Biological), were added into each well. After incubation at 37°C for 60 min the plat was rinsed with PBST and then incubated with secondary antibodies conjugated with HRP (109-035-003, Jackson ImmunoResearch) at 37°C for 30 min. After final rinses with PBST, TMB buffer (PR1200, Solarbio) was added. The reaction was quenched with 2N H_2SO_4. The plate was read in SpectraMax i3x and tested for absorbance at 450 nm. In blocking assay, anti-LILRB4/anti-Gal-8 antibody were pre-incubated with Fc-tagged LILRB4 protein and added to ELISA plate coated with 0.5 μg/mL Gal-8. The IC50 values of the antibodies were calculated accordingly. The Gal-8 detecting ELISA kit was developed using two anti-Gal-8 antibodies with different epitopes. One was coated on the ELISA plate, while the other was labeled with biotin (E-LK-B002, Elabscience) and used as the first antibody. Streptavidin-HRP (M00091, GeneScript) were then added to generate TMB signals. Recombinant Gal-8 protein was used to build a standard curve.

Immunofluorescence

The HEK293 cells were seeded in 8-well chamber slides (C7182, Sigma-Aldrich) and transfected with ectopic Flag-tagged Gal-8, Fc-tagged Gal-8 and/or HA-tagged LILRB4 plasmids with FuGENE HD (E2312, Promega). After 48 h, the cells were washed twice with PBS and fixed with 4% formaldehyde (P1110, Solarbio) for 20 min. After being washed twice with PBS, cells were permeabilized and blocked with 0.2% Triton X-100 (93443, Sigma-Aldrich) and 1% BSA in PBS simultaneously at room temperature (RT) for 1h. The cells were incubated with primary antibodies at 4°C overnight and with secondary antibodies for 20 min at RT. The staining antibodies included the following: anti-DYKDDDDK Tag (8146S, CST), anti-HA tag (3724S, CST), AF488-conjugated anti-mouse IgG (A-21202, Invitrogen), AF594-conjugated anti-rabbit IgG (A-21207, Invitrogen) and AF488-conjugated anti-human IgG (A-11013, Invitrogen). After the final rinses with PBS, the slides were sealed with DAPI Fluoromount-G (0100-20, SounthernBiotech) and observed under a fluorescence microscope. Quantification of fluorescence intensity and co-localization was performed using ImageJ software (version 2.0.0-rc- 69/1.52p).

Co-immunoprecipitation

The HEK293 cells were transfected with ectopic Flag-tagged Gal-8 and HA-tagged LILRB4 plasmids with FuGENE HD. After 48 h, the cells were harvested and lysed with IP Lysis Buffer (87787, Thermo Scientific) supplemented with a 1% cocktail of proteinase and phosphatase inhibitor and PMSF (KC-440, Aksomics). The cell lysates were centrifuged for 2 min at 12000 rpm at 4°C. After DNase (EN33-050, QIAGEN) treatment for 16 min at RT, 16 μL volume was collected from each sample (total volume 300 μL) and mixed with 4 μL 5×SDS-PAGE loading buffer (0015, Beyotime) to serve as the input control. The rest was incubated with 1 μg the following antibodies: anti-DYKDDDDK Tag (8146S, CST), anti-HA tag (3724S, CST), Mouse IgG Isotype (A7028, Beyotime), and Rabbit IgG Isotype (A7016, Beyotime). Protein G Agarose beads (20398, Thermo Scientific) were simultaneously incubated with 4% BSA for blocking. After incubation overnight at 4°C with slow rotation, each sample was added with an equal volume of beads and again incubated with rotation at RT for 1h. The samples were washed 3–4 times with PBS with high-speed rotation, mixed with 30 μL non-ruducing sample buffer (39001, Thermo Scientific), and heated at 100°C for 8 min. The samples were then analyzed by western blotting and detected with the following antibodies: anti-DYKDDDDK Tag (14793S, CST), anti-HA tag (sc-7392, Santa Cruz), HRP-conjugated anti-mouse IgG (KC-MM-035, Aksomics), HRP-conjugated anti-rabbit IgG (KC-RB-035, Aksomics).

BLI affinity and epitope binning assay

For affinity assay of Gal-8 and LILRB4, the recombinant Fc-tagged LILRB4 ECD protein was immobilized to the hFc probes (160003, Gator Bio) and incubated with Gal-8 protein in serial dilution. For affinity assay of anti-LILRB4 and anti-Gal-8 antibodies, the antibodies were immobilized to the Protein A probes (160001, Gator Bio) and incubated with antigens, the His-tagged LILRB4 or untagged Gal-8, in serial dilution. The affinity constants were calculated from a global fit of data obtained from the association and dissociation phase with a 2-fold concentration series. For epitope binning assay, each antibody was sequentially immobilized to the Protein A Probe and incubated first with His-tagged LILRB4 (Step1) and then with other antibodies (Step2). The generator biolayer interferometry system and data processing platform were utilized per the manufacturer's instructions (SNGC00070, Gator Bio). The epitope binning of anti-Gal-8 antibodies was performed as described and the data was visualized by Cytoscape 3.9.

Protein cross-linking and SDS-PAGE silver staining

Recombinant Gal-8 and LILRB4-his protein (16742-H08H, Sino Biological) were mixed in a 1:1 ratio of moles at 37°C for 30 min and incubated for 5 min at RT with Glutaric dialdehyde of indicated concentrations. The samples were then electrophoresed in SDS-PAGE (PG212, Epizyme) and silver-stained (P0017S, Beyotime).

Induction and detection of MDSCs

The cryopreserved PBMCs were resuscitated and treated with recombinant Gal-8/APOE proteins or PBS in the presence of 10 nM GM-CSF. After incubation for 3 days, the cells were washed twice with flow cytometry staining buffer (00-4222-26, Invitrogen) and incubated with Fc blocker (422301, BioLegend) and Zombie-Dye reagent (423102, Biolegend). Then the cells were stained with the following antibodies: anti-CD11b-APC (17-0112-82, Invitrogen), anti-human CD33-PE (303404, Biolegend) and anti-human HLA-DR-APC/Cy7 (100236, Biolegend). After washing three times with staining buffer, the samples were analyzed using MACSQuant16 (Miltenyi). The FlowJo V10 software was used to analyze the data.

T cell proliferation assay

$CD14^+$ monocytes were isolated from cryopreserved PBMCs using a positive selection kit (100–0694, StemCell), and treated with or without Gal-8 for 3 days, with the presence of GM-CSF. T cells were enriched from PBMCs and labeled with CFSE (C34554, Invitrogen). The labeled T cells were plated in the presence of 1 μg/mL anti-CD3 (14-0037-82, Invitrogen) and 1 μg/mL anti-CD28 (16-0289-81, Invitrogen) antibodies with 50 IU/mL IL-2 (200-02, Peprotech) at a 1:1 ratio with Gal-8 treated (and untreated) $CD14^+$ cells. After 5 days of coculture, cell samples were harvested, labeled with anti-CD3-APC (100236, Biolegend), and detected by flow cytometry. The percentage of decreased proliferation rate compared to the control group (whose suppression rate was zero) was calculated as suppression rate.

Transcriptome, morphology and cytokine analysis of immune cells

$CD14^+$ monocytes were isolated from cryopreserved PBMCs using a positive selection kit (100–0694, StemCell), and treated with or without Gal-8, with the presence of GM-CSF. After incubation for three days, the cells were observed with a microscope and morphological changes were recorded. Afterward, cells were collected, washed twice with PBS, lysed with TRIzol reagent (15596026, Invitrogen) and sent for sequencing (MRNA232620SH, Sangon). cell supernatants were used to detect IL-10 levels (SEKH-0018, Solarbio).

Establishment of stable cells

Ectopic Flag-tagged Gal-8 or HA-tagged LILRB4 plasmids were transfected into Mc38, B16, or HEK293 cells using FuGENE HD Transfection Reagent (E2312, Promega). A blank vector control was used. After approximately two weeks of incubation supplemented with 200/350/600 μg/mL (for different cell types respectively) G418 (10131027, Gibco) with refreshing the medium every 2–3 days, single colonies were picked and verified by immunoblotting. An optimal clone was selected and expanded. THP-1 cells

were transfected with lentiviruse with LILRB4 shRNA (GIEL0223634, GeneChem). Transfection was performed according to the manufacturer's instructions. After 96 h, the medium was replaced with RPMI-1640 complete medium containing 2 μg/mL puromycin (ant-pr, InvivoGen). The medium was refreshed every 2–3 days for two weeks, and transfection efficiency was determined by immunoblotting.

Immunoblotting and nuclear extraction

For whole-cell protein assay, cells were lysed with RIPA buffer (89901, Thermo Scientific) supplemented with 1% proteinase and phosphatase inhibitor cocktail. The collected cell lysates were centrifuged for 15 min at 12000 rpm, 4°C. The supernatant was preserved, and the protein concentration was determined using a BCA Protein Assay Kit (P0010, Beyotime). 5×SDS-PAGE loading buffer was diluted with protein sample and heated at 100°C for 8 min. For Nuclear and cytoplasmic extraction assay, the cells were processed per manufacturer's instructions (78833, Thermo Scientific). The protein extracts were subjected to SDS–PAGE at appropriate concentrations for electrophoresis and transferred to PVDF membranes (1620177, Bio-Rad). For dot blotting assay, 2 μL cell lysates were added onto activated PVDF membranes dropwise and left to dry at room temperature. Membranes were blocked with blocking buffer (PS108, Epizyme) for 5 min at RT and then incubated overnight at 4°C with the following antibodies: anti-phospho-SHIP-1 (3941T, CST), anti-SHIP-1 (sc-8425, Santa Cruz), anti-phospho-SHP-1 (8849T, CST), anti-SHP-1 (sc-7289, Santa Cruz), anti-phospho-SHP-2 (3751T, CST), anti-SHP-2 (sc-7384, Santa Cruz), anti-phospho-STAT3 (Tyr705) (9145S, CST), anti-phospho-STAT3 (Ser727) (9134S, CST), anti-STAT3 (9139S, CST), anti-phospho-NF-κB p65 (3033S, CST), anti-NF-κB p65 (8242S, CST), anti-phospho-AKT (4060S, CST), anti-AKT (4691S, CST), anti-phospho-ERK 1/2 (sc-81492, Santa Cruz), anti-SHP-2 (sc-514302, Santa Cruz), anti-LILRB4 (GTX33296, GeneTex), anti-LGALS8 (orb216142, Biorbyt), anti-SOCS3 (ab16030, Abcam), HRP-conjugated anti-GAPDH (KC-5G5, Aksomics), HRP-conjugated anti-β-Actin (KC-5A08, Aksomics), anti-S100A8 (15792-1-AP,ProteinTech), anti-S100A9 (26992-1-AP,ProteinTech), anti-ADAM17(ab2051,Abcam), anti-PD-L1 (13684S, CST), anti-CD163 (333602, Biolegend), anti-α-Tubulin (AF7010, Affinity), anti-Lamin B (12586T, CST). After rinses with TBST (TBS, 0.1% Tween 20) (B548105, Sangon), the PVDF membranes were incubated with secondary HRP-conjugated antibodies at RT for 1 h. The membranes were washed five times with TBST and examined using the ECL Detection Reagent (36208ES60, Yeasen) with the ChemiDoc imaging system (Bio-Rad).

Ubiquitination assay of TRAF-6

THP-1 cells were treated with or without Gal-8 for 48 h and the transfected THP-1 cells were harvested without treatment. The protein extraction and processing steps were the same as for immunoprecipitation. The antibody used to precipitate the protein was anti-TRAF6 antibody (8028T, CST). The samples were then analyzed by western blotting and detected with anti-K63-linkage specific poly-ubiquitin antibody (5621T, CST).

Membrane and soluble IL-6R assay

THP-1 cells were treated with or without Gal-8 for three days before IL-6R assays. Membrane expression was detected with flow cytometry assay, using anti-IL-6R-PE/Cy7 antibody and Mouse IgG1-PE/Cy7 Isotype. Supernatants were collected and tested with ELISA kit (E-EL-H2518, Elabscience).

Reporter cell assay

THP-1 reporter cells were treated with Pam3CSK4 (tlrl-pms, InvivoGen) for activation and cocultred with stably transfected HEK293 cells. After 18 h of incubation at 37°C under 5% CO2. A volume of 20 μL volume per well was collected and mixed with 180 μL Quanti-blue solution (rep-qbs, InvivoGen) to a flat bottom 96-well plate. The plate was placed in SpectraMax i3x and tested for absorbance at 630 nm. The measurements were immediately performed and the entire process was protected from light.

Flow cytometry assay

For membrane protein variation assay, THP-1 or $CD14^+$ cells were incubated with Fc blocker reagent and Zombie viability dye, before being stained with the following antibodies, anti-ADAM17(ab2051, Abcam), anti-PD-L1 (13684S, CST), anti-CD163 (333602, Biolegend), Anti-rabbit IgG-PE (333602, Biolegend) and anti-mouse IgG AF488. For antibody affinity assay on cell lines, anti-Gal-8 antibodies were incubated with permeabilized cells and stained with AF647-conjugated anti-Human IgG antibody (A-21445, Invitrogen).

Epitope mapping

Alanine scanning assay was used to map the binding epitope of Clone 3–11 antibody to LILRB4. Briefly, the amino acid sequence of the LILRB4 extracellular domain was used to design 11 peptides with overlapping ends and a length of 27 amino acids. After ELISA assay, P10 was shown to bind clocking antibodies. The 27 amino acid residues of P10 were sequentially mutated to alanine, yielding 27 different polypeptides for ELISA assays.

Antibody fab production

The anti-LILRB4 antibody Clone 4–25 were processed with the Fab preparation kit (44985, Thermo Scientific). The components of the production process were collected and detected by Coomassie blue staining (P0017A, Beyotime) of SDS-PAGE.

In vivo tumor models of phenotypes

After one week of adaptation to the environment, C57BL/6 lilrb4-KO (C57BL/6Smoc-Lilrb4a^{em1Smoc}) (NM-KO-200727, SMOC) and C57BL/6Smoc mice (SM-001, SMOC) (female/male, six weeks old) was randomized into four groups (n = 5/n = 8 for different batches). Stably transfected B16 cells were injected subcutaneously in the right flank (the establishment of stable cell clones as described later) at 3 × 10^5 per individual. When tumors became measurable, the tumor sizes were recorded every 2 days using a Vernier caliper and calculated using the formula 1/2 × A × a^2 (A and a denote the length and width of the tumor, respectively). Per ethical guidelines, mice were sacrificed once the tumor volume reached 2000 mm^3 or ulcers occurred.

In vivo tumor models of therapeutic effects

For the anti-LILRB4 therapy in humanized-LILRB4 model, the same numbers of B16-Gal-8 OE cells were injected subcutaneously in humanized-LILRB4 mice (C57BL/6Smoc-Lilrb4a$^{em1(hLILRB4)Smoc}$) (NM-HU-210024, SMOC). When the tumors became measurable, the mice were grouped evenly according to tumor size and body weight (n = 5). Clone 4–25 antibody or Isotype IgG were given intraperitoneally every 2 days since the tumor size reached 100 mm^3. The measuring method and endpoint criteria were as previously described. Samples were collected as described. For the comparison of anti-Gal-8 and anti-LILRB4 therapy in humanized models, PBMCs were mixed with 2.1 × 10^6 of A375 cells or 2.4 × 10^6 of Hct116 cells at a 1:4 ratio and injected subcutaneously into each NCG mouse (T001475, Gempharmatech). The mice were grouped according to tumor size and body weight and then received PBS (vehicle), Clone A269 antibody (anti-Gal-8), and Clone 4–25 antibody (anti-LILRB4) treatment. When the tumors became measurable, the mice were grouped evenly according to tumor size and body weight (n = 6). Antibody administration and tumor measurements were performed as described previously.

Flow cytometry analysis of *In vivo* tumor models

Tumors were minced and incubated for 30 min at 37°C in 2 mL digestion buffer (1 mg/mL collagenase (C2674, Sigma-Aldrich) and 100 μg/mL DNase I (D4527, Sigma-Aldrich) in RPMI 1640 medium). Cell suspensions were passed through a 100 μm cell strainer. After waching with RPMI 1640, cells were resuspended in 40% Percoll (17089101, Cytiva) and centrifuged. After centrifugation, Cells were washed with staining buffer.Spleens were minced and rinsed with 5 mM EDTA in RPMI 1640. Peripheral blood were obtained from mouse eyeballs and treated with anticoagulant reagent (G0280, Solarbio). Erythrocytes were lysed with 1 mL of ACK Lysing Buffer (C3702, Beyotime) per spleen for 2 min. Splenocytes and PBMCs were washed with RPMI 1640, centrifuged, followed by rinsing with staining buffer. After centrifugation, cells were resuspended in PBS at 1 × 10^8 cells/mL and incubated with anti-mouse CD16/32 antibody (101302, Biolegend) and viability dye for 15 min at RT. Then, cells were stained with anti-CD11b-APC, anti-Ly-6C-FITC (128006, Biolegend) and anti-Ly-6G-PerCP/Cy5.5 (127616, Biolegend) antibody.

Immunohistochemistry

Tumors were dissected from *in vivo* models and deparaffinized and rehydrated, and antigen retrieval was performed using a citrate antigen retrieval solution (P0081, Beyotime). Melanoma tissue microarray slide was purchased from Xi'an Taibs Biotechnology (MME1004i, TaibsBio). After incubation with endogenous peroxidase with 3% H2O2 for 15 min and with goat serum for 1 h, tissue samples were incubated with anti-mouse CD8 (ab217344, Abcam), anti-mouse FOXP3 (12653S, CST) and anti-Gal-8 (ab109519, Abcam) antibodies overnight at 4°C, followed by incubation with HRP-conjugated secondary antibodies (D3004, Changdao) at RT for 1 h. DAB was used as a chromogen (P0203, Beyotime), and nuclei were counterstained with hematoxylin (Beyotime, C0105S). For CD8 and FOXP3 analysis, the number of positive cells was manually counted in 5 random scopes per slide. By scoring the area and intensity of positivity separately and calculating the total score, the expression of Gal-8 in melanoma tissues were classified into four levels. The area score included 5 levels: 0 (<5%), 1(5%–25%), 2 (25%–50%), 3 (50%–75%) and 4 (>75%). The intensity score included 4 levels: 0 (Negative), 1 (Low), 2 (Moderate) and 3 (High).

QUANTIFICATION AND STATISTICAL ANALYSIS

Column bar graphs and scatterplots were plotted using GraphPad Prism 9. Values were presented as the mean ± SEM from at least three independent experiments. Two-sided Student's *t* test was applied to compare two independent samples and a one-way analysis of variance with a post hoc test (Tukey) was applied to compare more than two groups. ImageJ (V.2.0.0-rc-69/1.52p) was used to quantify immunofluorescence and Western blot analyses. The co-localization factor (Pearson's R value) was calculated using ImageJ with the plugin 'coloc2' to evaluate the co-localization between two proteins. The number of samples assigned to each treatment was selected to provide sufficient statistical power to discern significant differences between groups based on prior experience with the experiment. The only data points excluded were clear outliers due to technical problems in assays performed in triplicate experiments. In this work, a p value <0.05 was considered statistically significant.